UNCLASSIFIED

SECURITY CLASSIFICATION OF THIS PAGE *(When Data Entered)*

REPORT DOCUMENTATION PAGE		READ INSTRUCTIONS BEFORE COMPLETING FORM
1. REPORT NUMBER TECHNICAL REPORT ARBRL-TR-02564	2. GOVT ACCESSION NO.	3. RECIPIENT'S CATALOG NUMBER
4. TITLE *(and Subtitle)* Computational and Experimental Studies of Blockage Effects in a Blast Simulator		5. TYPE OF REPORT & PERIOD COVERED Final (Dec 82 - Mar 83) 6. PERFORMING ORG. REPORT NUMBER
7. AUTHOR*(s)* Noel H. Ethridge, Richard E. Lottero John D. Wortman, Brian P. Bertrand		8. CONTRACT OR GRANT NUMBER*(s)*
9. PERFORMING ORGANIZATION NAME AND ADDRESS US Army Ballistic Research Laboratory, ARDC ATTN: DRSMC-BLT(A) Aberdeen Proving Ground, MD 21005		10. PROGRAM ELEMENT, PROJECT, TASK AREA & WORK UNIT NUMBERS 1L162618AH80
11. CONTROLLING OFFICE NAME AND ADDRESS US Army AMCCOM, ARDC Ballistic Research Laboratory, ATTN: DRSMC-BLA-S(A) Aberdeen Proving Ground, MD 21005		12. REPORT DATE June 1984 13. NUMBER OF PAGES 64
14. MONITORING AGENCY NAME & ADDRESS*(if different from Controlling Office)*		15. SECURITY CLASS. *(of this report)* UNCLASSIFIED 15a. DECLASSIFICATION/DOWNGRADING SCHEDULE

16. DISTRIBUTION STATEMENT *(of this Report)*

Approved for public release, distribution unlimited.

17. DISTRIBUTION STATEMENT *(of the abstract entered in Block 20, if different from Report)*

18. SUPPLEMENTARY NOTES

19. KEY WORDS *(Continue on reverse side if necessary and identify by block number)*

Blast loading	Shock tube flow	Wind tunnel blockage
HULL hydrocode	Dynamic pressure	Blockage compensation
Shock tube	Vehicle overturning	Free-flight experiments
Blast simulator	Nozzle theory	Blast simulator design
Blockage effects	Choking	

20. ABSTRACT *(Continue on reverse side if necessary and identify by block number)*

The confinement of a target by the walls of a blast simulator produces changes in the loading experienced by the target. The changes increase in magnitude with the blockage ratio, the ratio of target area to the simulator cross-sectional area. Computations were made using the HULL hydrocode in an axisymmetric configuration for non-decaying waves for different blockage ratios for a cylindrical target. It was found that the flow in the constricted region between the target and the shock tube wall was typically accelerated to velocities greater than the steady flow values behind the

DD FORM 1 JAN 73 1473 EDITION OF 1 NOV 65 IS OBSOLETE

UNCLASSIFIED

SECURITY CLASSIFICATION OF THIS PAGE *(When Data Entered)*

incident shock in an unobstructed shock tube. The net axial load on the target computed from the hydrocode results could be related directly to the dynamic pressure in the constricted region, which increased as the blockage was increased. This meant that non-decaying shocks which did not produce net loads sufficient to overturn a target in a shock tube at low blockage could be made to do so by increasing blockage while keeping shock overpressure constant. Thus, tests where the blockage is high can be misleading unless corrections are made for the effect of blockage. The step shock computations provided an extreme case for analysis; similar computations were performed for the other extreme case of a rapidly decaying wave. Although critical flow parameters in the constricted region (e.g., particle velocity and dynamic pressure) were similarly increased for the decaying wave, the effect on the net force was found to be small. This was because of the overpressure gradient across the target and the reduced importance of drag loading compared to diffraction phase loading. Predictions of the increase in dynamic pressure in the constricted region with increasing blockage ratio were made using the theory for an ideal converging-diverging nozzle. The late-time steady-flow conditions for a step shock were simulated. These results agreed well with HULL hydrocode calculations and showed when choking conditions occur. Flow configurations at the target were derived from the HULL computations and show large variations in dynamic pressure near the vicinity of the target. Shock tube experiments were performed to determine drag force on cylindrical targets versus blockage ratio. The results confirmed that large increases in axial loading occur at blockage ratios of 0.2 and 0.3. Wind tunnel experiments with models at low speed and blockage ratios up to 0.15 showed increases in drag force with blockage ratio in good agreement with HULL results. Compensation techniques are considered. One involves reduction of input blast wave duration to maintain the same effective drag impulse as would occur for no blockage. Another technique recommended for further study is the use of vent ports in the test section walls surrounding the target.

AD

TECHNICAL REPORT ARBRL-TR-02564

COMPUTATIONAL AND EXPERIMENTAL STUDIES OF BLOCKAGE EFFECTS IN A BLAST SIMULATOR

Noel H. Ethridge
Richard E. Lottero
John D. Wortman
Brian P. Bertrand

June 1984

US ARMY ARMAMENT RESEARCH AND DEVELOPMENT CENTER
BALLISTIC RESEARCH LABORATORY
ABERDEEN PROVING GROUND, MARYLAND

Destroy this report when it is no longer needed.
Do not return it to the originator.

Additional copies of this report may be obtained from the National Technical Information Service, U. S. Department of Commerce, Springfield, Virginia 22161.

The findings in this report are not to be construed as an official Department of the Army position, unless so designated by other authorized documents.

The use of trade names or manufacturers' names in this report does not constitute indorsement of any commercial product.

PREFACE

Material in this report was accepted for presentation at MABS-8, the Eighth International Symposium on Military Applications of Blast Simulation, in Spiez, Switzerland, 20-24 June, 1983, and was published in the Proceedings of the Symposium under the title "Blockage Effects in a Large Blast Simulator."

TABLE OF CONTENTS

LIST OF ILLUSTRATIONS

LIST OF ILLUSTRATIONS (Continued)

LIST OF TABLES

I. INTRODUCTION

The US Army Ballistic Research Laboratory (BRL) is designing a large shock tube to produce blast loading equivalent to that from large explosions on full size targets (e.g., trucks carrying communication shelters). Such a target in a shock tube presents an obstruction to the flow behind the shock. The walls of the tube confine the flow and reflect waves produced by the shock wave interaction with the target. The loading on the target is changed from that which would occur under free-field conditions. The changes increase in magnitude with the blockage ratio, B, the ratio of target cross-sectional area to the blast simulator cross-sectional area. Studies of blockage effects have been made at BRL to provide guidance for the design of a large blast simulator.

The purpose of this paper is to present the results of such studies, which have included applications of nozzle theory, HULL hydrocode computations, shock tube experiments, and comparison with published wind tunnel data.

II. NOZZLE THEORY

A target in a shock tube causes a constriction of the area open for flow* in the tube, which can significantly change the flow field around the target from that for a free-field encounter with the same shock wave. The flow immediately upstream from the target is modified by the reflected shock, which decelerates the flow and increases its stagnation temperature and decreases its stagnation pressure. These effects caused by the reflected shock are greater in a shock tube than in the free field because the reflected shock is prevented from free expansion by the shock tube walls. After several crossing times,** the effects of the reflected shock are diminished; and, in the case of a non-decaying (step) shock, a steady-state flow develops, lasting until the arrival of the contact discontinuity which separates the driver gas from the driven gas. This limiting case of a long-duration step shock offers an opportunity to analyze the late-time effects of blockage, particularly in regard to the enhancement of the net force due to drag.

Many targets of interest to the Army are box-like, typifying those tested in shock tubes at the BRL. The target blocks the flow behind the shock, slowing and recompressing it. The flow then accelerates around the target and expands after passing it. In this respect, the tube-and-target geometry crudely resembles a converging-diverging nozzle, with the constricted-flow region between the target and the tube walls functioning as the throat. In nozzle theory the flow is assumed to be one-dimensional and steady. The condition of one-dimensionality in the tube-and-target case is

The constricted-flow region is between the target and the shock tube wall.
**A crossing time is the time that the incident shock takes to traverse the length of the target.*

violated for all time, and the steady flow condition is only approximated at late time for a step shock. Nonetheless, the use of nozzle theory serves as a useful guide in providing theoretical limits for flow variables near the target. The conditions in this "throat" area are indicators of the effect of blockage on the flow around the target, and hence the change in the loading on the target compared with that for a free-field encounter. A useful indicator of the flow in the throat region is the average local Mach number in the effective throat area. The analytical relations for an ideal (De Laval) converging-diverging nozzle,[1] using the late-time stagnation conditions as "reservoir" conditions, can be used to generate a set of curves indicating lower bounds for local throat Mach number. (The Mach number is the particle velocity magnitude divided by the speed of sound.) These bounds are shown for several shock strengths in Figure 1, plotted as functions of B. The blockage ratio may be redefined in terms of nozzle geometry as

$$B = 1 - \frac{A_t}{A_i}, \tag{1}$$

where

A_t = nozzle throat area (constricted region area), and

A_i = nozzle inlet area (test section area).

Thus, B retains the same definition as for the blast simulator with blockage if it is further understood that

$$\text{Target Area} = A_i - A_t, \tag{2}$$

and the nozzle inlet area and blast simulator test section area are the same. As may be seen in Figure 1, the local Mach number behind the incident shock is quite high for shocks above 172.4 kPa (25 psi), with choking occurring at $B \geq 0.11$.

Choking is most properly defined for quasi-one-dimensional flow in a nozzle. There, choking occurs when the throat Mach number equals unity. A broadened use of the definition of choking is used in this study to characterize the flow in the constricted region between the target and the shock tube wall. The local Mach number in that region is defined in terms of the axial component of velocity and the local speed of sound. The specific radial cut across that region is discussed in detail later.

Another very informative way of looking at the effect of blockage on the local Mach number in the throat is to normalize it by dividing by the local Mach number behind the incident shock. The resulting Mach number ratio, M_R,

---

[1] *A.H. Shapiro, The Dynamics and Thermodynamics of Compressible Fluid Flow, Volumes I and II, Chpts 2, 4, and 25, The Ronald Press Company, New York, New York, 1953.*

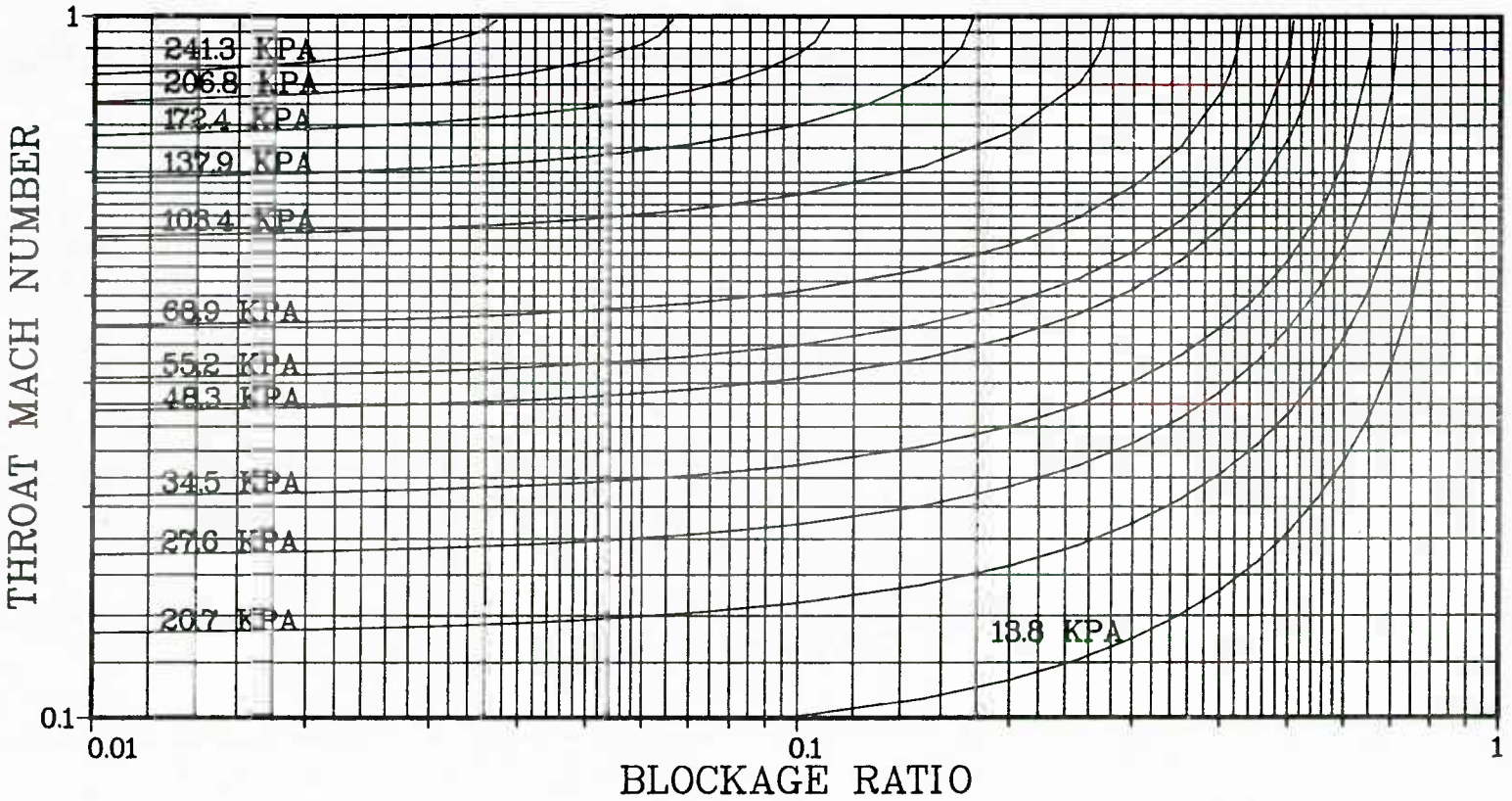

Figure 1. Local throat Mach number versus blockage ratio for an ideal converging-diverging nozzle for several late-time flows behind step shocks.

then gives a relative measure of the difference in the flow near the target compared with the flow behind the incident shock prior to its interaction with the target. The data plotted in Figure 1 were normalized in this fashion and are shown in Figure 2. The curves successively rise from a lower bounding curve that would be generated for a shock of infinitesimal strength. The choking limit is that point at which the curve becomes suddenly flat, having a discontinuity in its first derivative. The stronger the shock, the sooner the curve rises from the lower bounding curve and goes to a choked condition. The low-blockage region of Figure 2 near B=0.01, corresponding to a small area reduction from nozzle inlet to throat, shows a small relative change from "free-field" conditions. As blockage is increased, the change in M_R increases at an increasing rate, indicating that the throat, or constricted-flow region, is experiencing very different flow from that which is upstream.

The dynamic pressure ratio*, Q_R, in the throat is a good indicator of the net load on a target. Figure 3 shows Q_R in the throat as a function of B for the same set of incident shock strengths. As was the case for the curves for M_R versus B, the curves for Q_R have a lower bounding curve, with the curves for the stronger shocks rising from it progressively sooner. The limits for choking are also shown by the abrupt transition to a constant value. Also shown in Figure 3 are the results from previously reported[2] hydrocode computations. These will be discussed in detail in the section entitled "HULL Hydrocode Computations" after the computations themselves are described.

The results from nozzle theory presented in Figures 1, 2, and 3 show when choking or near-choking conditions occur in the throat of an ideal converging-diverging nozzle for inviscid flow. Corresponding changes in other flow parameters are also indicated. These results may be used as guidelines for establishing limiting theoretical values against which the flow in an actual or simulated target-and-tube situation may be compared. This will also be discussed more fully in the section entitled "HULL Hydrocode Computations."

Dynamic pressure ratio is the dynamic pressure in the throat divided by the dynamic pressure behind the incident shock. Dynamic pressure is computed as $1/2\,\rho v^2$, where ρ is the density and v is the particle velocity.

[2] *N.H. Ethridge, R.E. Lottero, J.D. Wortman, and B.P. Bertrand, "Flow Blockage and its Effect on Minimum Incident Overpressures for Overturning Vehicles in a Large Blast Simulator," Proceedings of the Seventh International Symposium on Military Applications of Blast Simulation, Vol. II, Medicine Hat, Alberta, Canada, 13-17 July 1981.*

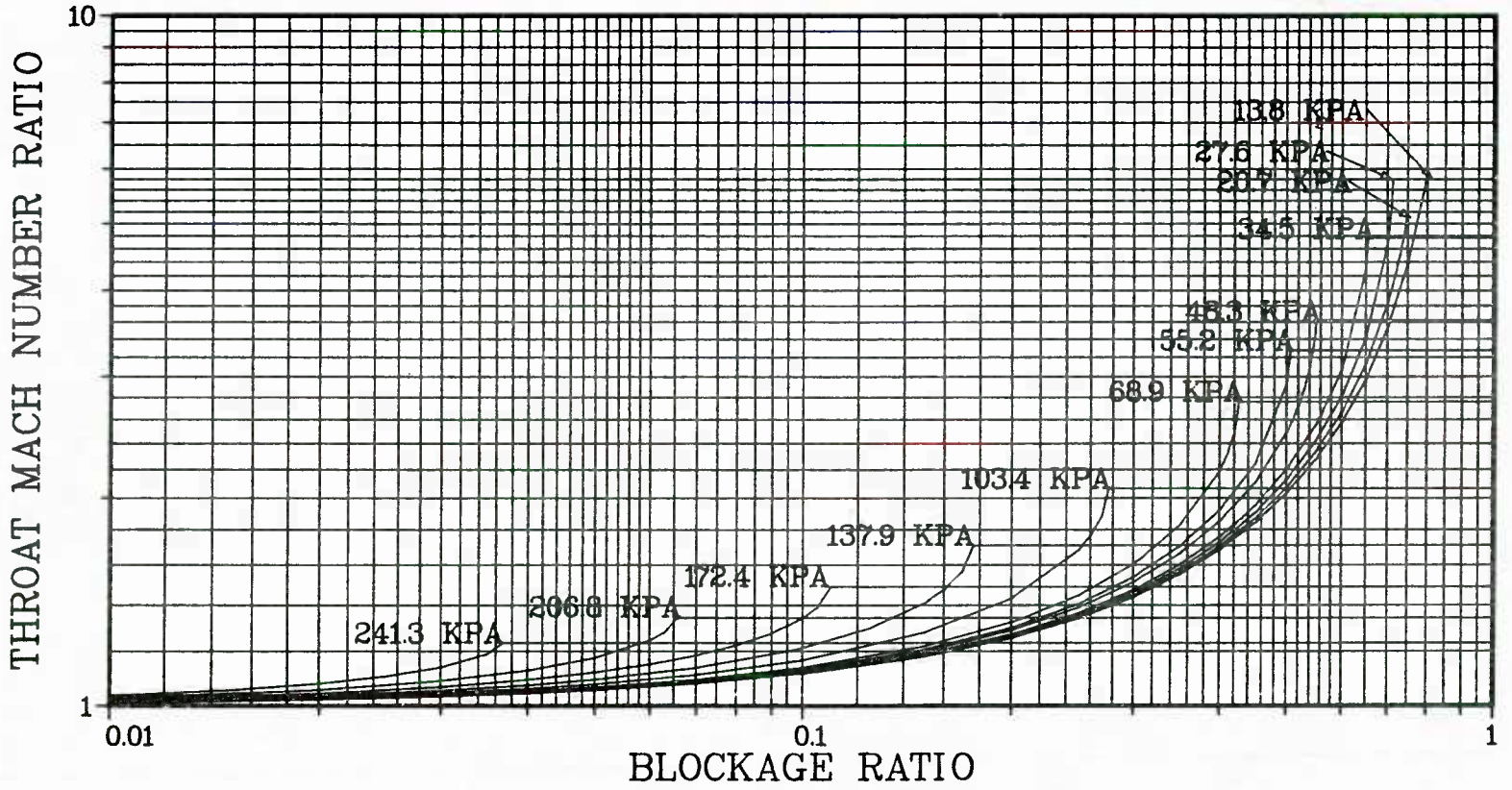

Figure 2. Local throat Mach number ratio versus blockage ratio for an ideal converging-diverging nozzle for several late-time flows behind step shocks, with the local Mach number behind the incident shock as the normalizing factor.

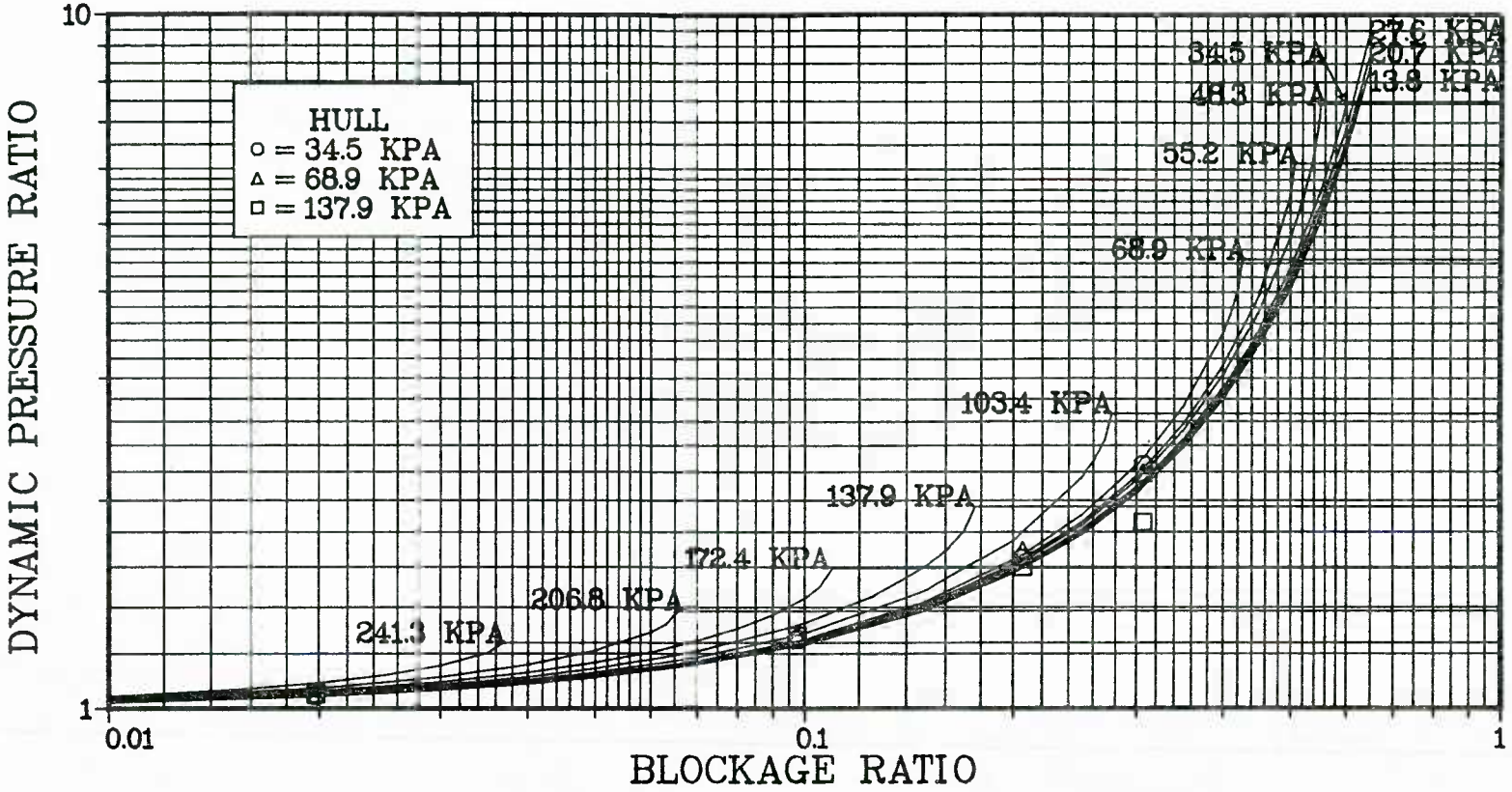

Figure 3. The ratio of dynamic pressure in the throat to dynamic pressure behind the incident shock versus blockage ratio for an ideal converging-diverging nozzle for several late-time flows behind step shocks, and from hydrocode computations.

III. HULL HYDROCODE COMPUTATIONS

A. Step Shock Computations

A previously reported study[2] conducted by BRL quantified the effect of shock tube blockage on the net axial loading of a simple target struck by a step shock wave. For that study, the two-dimensional cylindrical (axisymmetric) version of the HULL hydrocode was used to simulate a step shock wave striking a stationary, rigid cylindrical target having its axis coincident with the axis of a cylindrical shock tube. The area facing the shock and the length of the target were chosen to approximate that of a 2-1/2 ton truck carrying a communications shelter. Shocks with overpressures of 34.5 kPa (5.0 psi), 68.9 kPa (10.0 psi), and 137.9 kPa (20.0 psi) were simulated. Nominal values of blockage ratio B = 0.02, 0.1, 0.2, and 0.3 were used. The computations are discussed in detail in Reference 2 and so will only be summarized here to the extent required for clarity.

Figure 4 shows the flow field configuration modeled. All computations were performed for the same stationary, rigid cylindrical target. The left boundary of the flow field shown in Figure 4 is an axis of symmetry about which the entire flow field may be rotated to get a full view. Four different outer-radial boundary locations were used to simulate the four values of B quoted above. The outer-radial boundaries for B=0.1, 0.2, and 0.3 were simulated as being perfectly reflecting. Some cases were run for B=0.02 with that boundary perfectly reflecting and some with it transmissive for purposes of comparison.* Cases with B=0.02 were deemed to be essentially free field. The bottom boundary was set up to continuously input shocked air, and the top boundary was transmissive to allow the shock to pass out of the grid. The initial shock location in all computations was five computational flow field cells (0.545 m) upstream from the front face of the target cylinder. The shock was aligned so that its velocity vector was parallel to the axis of symmetry and hence normal to the front face of the target cylinder. The direction of travel of the shock was from bottom to top in Figure 4. In order that comparisons between the computations at different blockages would be as meaningful as possible, the lower blockage computational grids were designed so that they included the higher blockage grids as subsets. This meant that the computational grid immediately adjacent to the target was always the same from one computation to the next. Thus, any variation in the results because of changes in the target or changes in the spacing and resolution in the finite difference grid could be eliminated as factors for consideration because they do not exist.

A transmissive boundary simulates zero-gradient pressure and normal velocity component conditions to allow fluid to flow out of the grid. This, unfortunately, reflects a spurious weak wave of like kind when struck by an expansion, compression, or shock wave. The reflective and symmetry boundaries simulate a zero-gradient pressure and a zero normal velocity component (no flow).

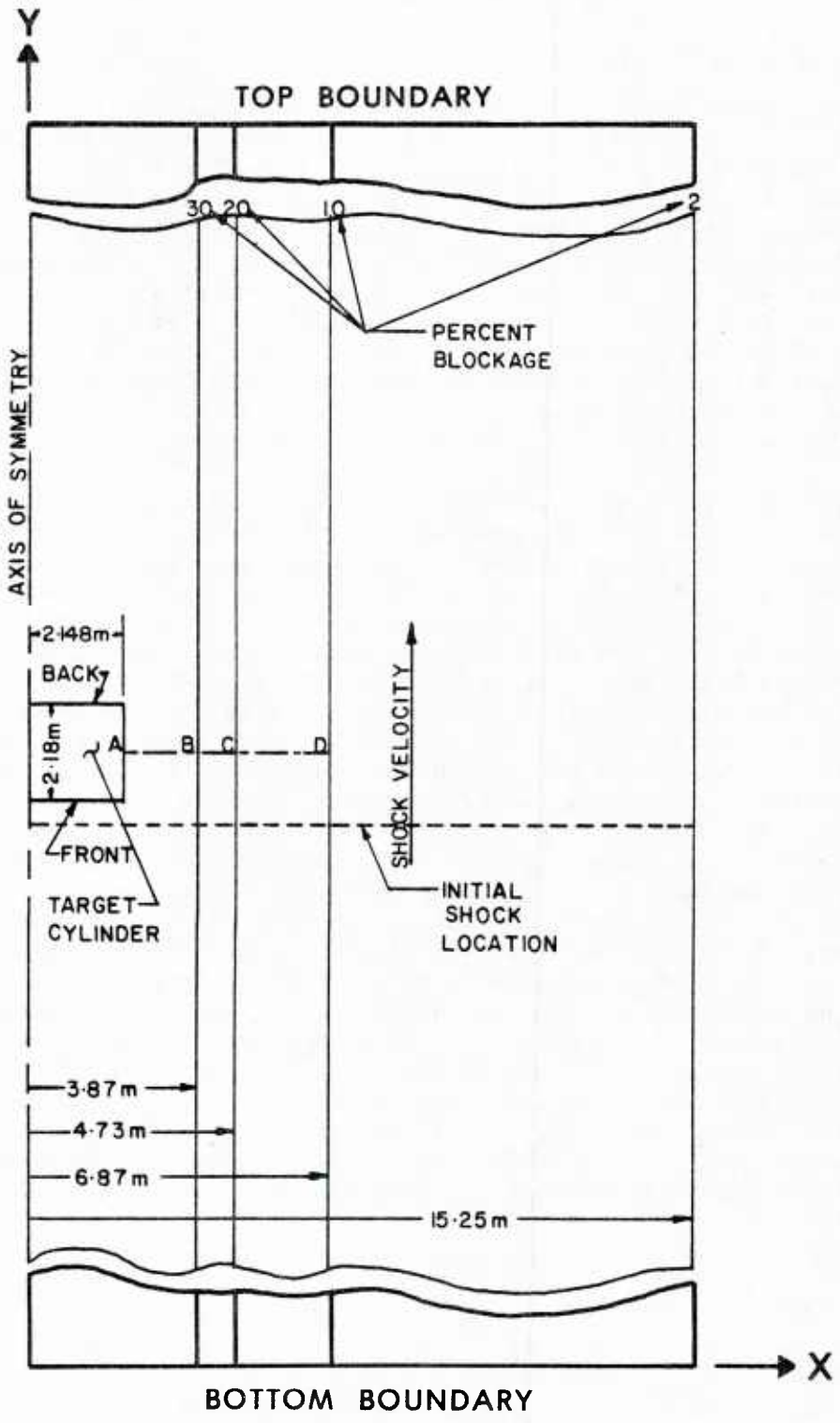

Figure 4. Target cylinder in computational flow fields.

The most significant effect of blockage on a target in a shock tube is the change in the net axial loading, which was shown by the computations to vary directly with blockage. The net axial loading on the target was computed from the hydrocode results by integrating the force on the front face of the target and subtracting from it a similarly-obtained integral on the back face. The results from the hydrocode computations on the back face may not be as accurate as those on the front face because the code does not model true viscous effects. However, it has been shown[2] that the results on the back face for this class of problem are of sufficient accuracy that they may be used for this purpose with confidence in their validity. The results of those computations for the 34.5 kPa shock are shown in Figure 5. The curve for 2 percent blockage shows the net axial loading on the target for essentially free-field conditions. This curve can be used to illustrate the two loading phases that occur during the interaction of a blast wave with a target. The first phase, the "diffraction" phase, is dominated by the initial shock interaction and engulfment of the target, and the subsequent relieving rarefaction waves. Once the diffraction phase ends, the "drag" phase begins. This is dominated by the flow behind the incident shock and shows little or no wave interaction. (The flow behind a non-decaying shock is a steady flow.) These two phases are shown distinctly in the curve for 2 percent blockage in Figure 5. The diffraction phase here lasts for approximately 20 ms and is dominated by the peak loading from the initial interaction and its subsequent relief. The drag phase then begins, reaching a relatively constant value by 35 ms. The curve for 10 percent blockage follows that for 2 percent blockage until shortly after the end of the diffraction phase. At that time, waves which reflected from the target have travelled to the outer-radial boundary, reflected from it, and returned to the target. The target is reloaded to a value nearly twice that for the 2 percent blockage case, is over-relieved to a lower value, and reloaded again. For 20 percent blockage, the returning waves arrived just before the end of the diffraction phase. There is a subsequent series of reflected wave arrivals and reliefs, oscillating about a line approximately 40 percent above that for free field. The curve for 30 percent blockage shows reflected waves arriving correspondingly sooner than those for 20 percent blockage but still late in the diffraction phase. The late time net axial load on the target is approximately twice that for a free-field encounter.

Figure 6 shows a similar set of curves for the 68.9 kPa step shock, and Figure 7 shows a similar set for the 137.9 kPa shock. The figures show clear trends of increasing net axial force in the drag phase with increasing blockage for each shock overpressure but relatively little effect in the diffraction phase.

Analysis of the computation also indicated that there were systematic increases with increasing blockage of the dynamic pressure in the constricted-flow region. Average values of dynamic pressure were computed by summing the product of the flow-field cell area times the dynamic pressure for each cell across the constricted-flow region, and dividing the sum by the total area. The plane at the mid-length of the cylindrical target was chosen for computing these average values. Figure 4 includes a schematic representation of the areas used for averaging. Section line AB shows an edge-on view of the ring-shaped area for averaging for 30 percent blockage, section line AC for 20 percent blockage, and section line AD for 10

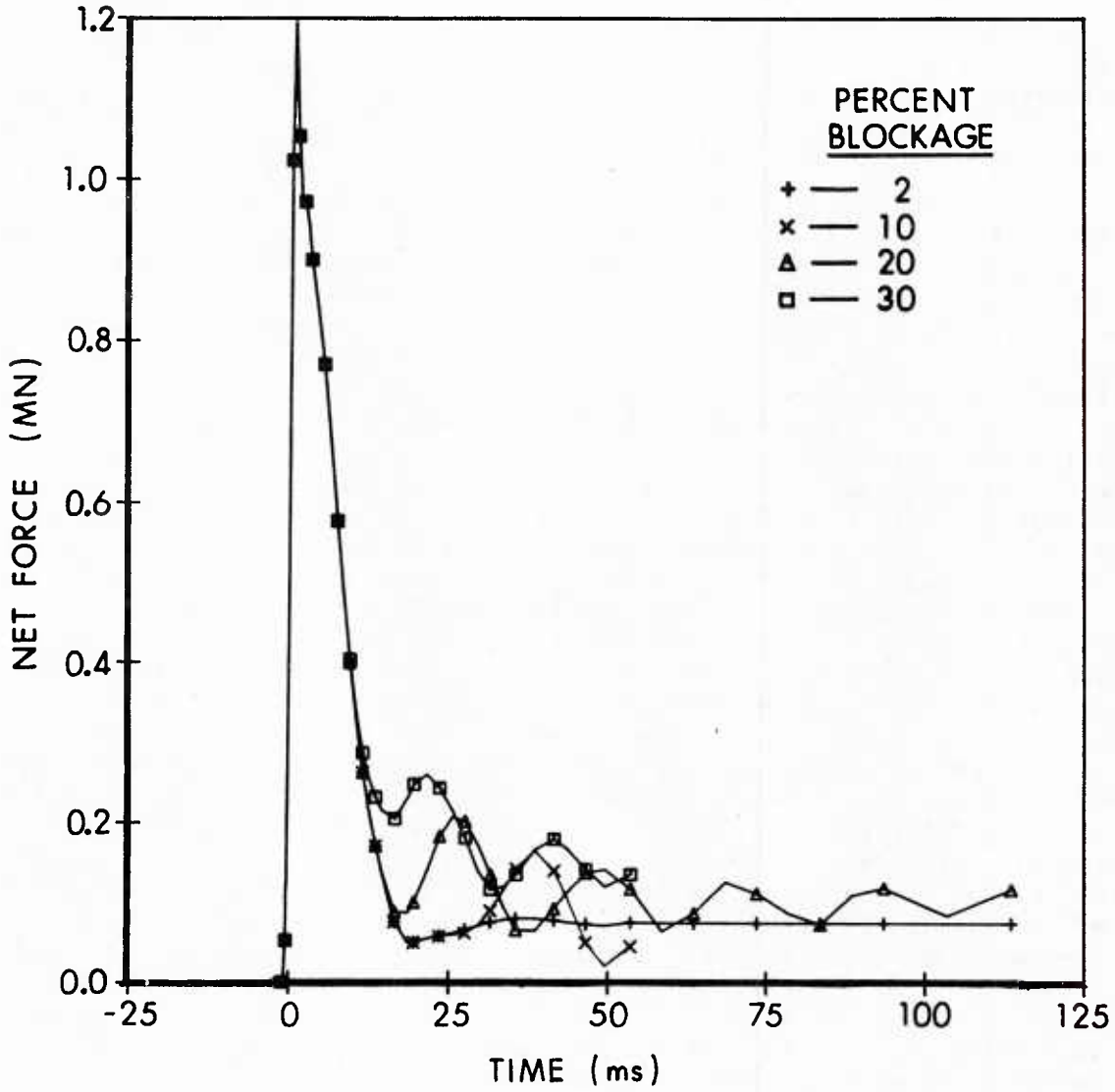

Figure 5. Net force on target cylinder for the 34.5 kPa shock.

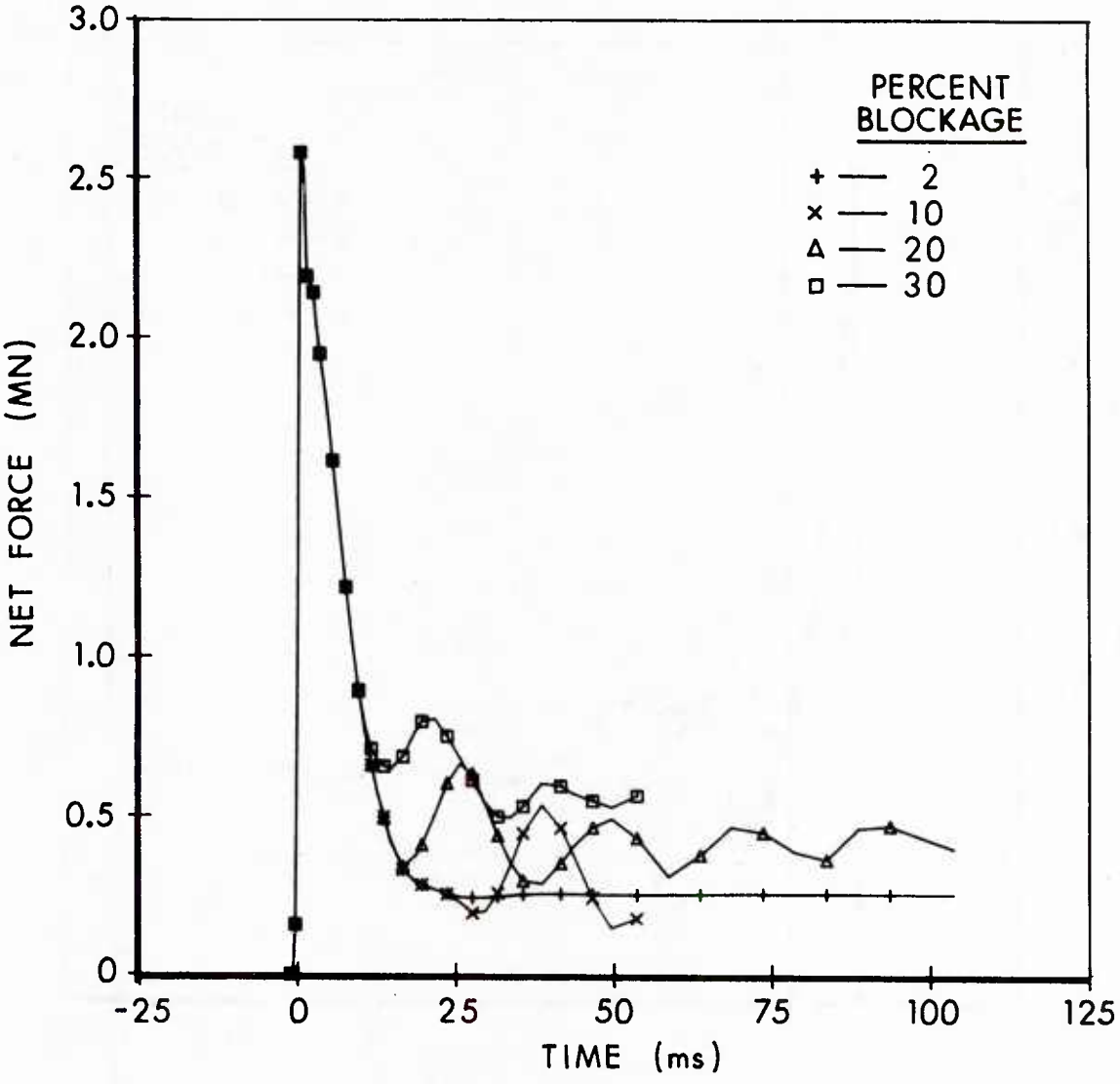

Figure 6. Net force on target cylinder for the 68.9 kPa shock.

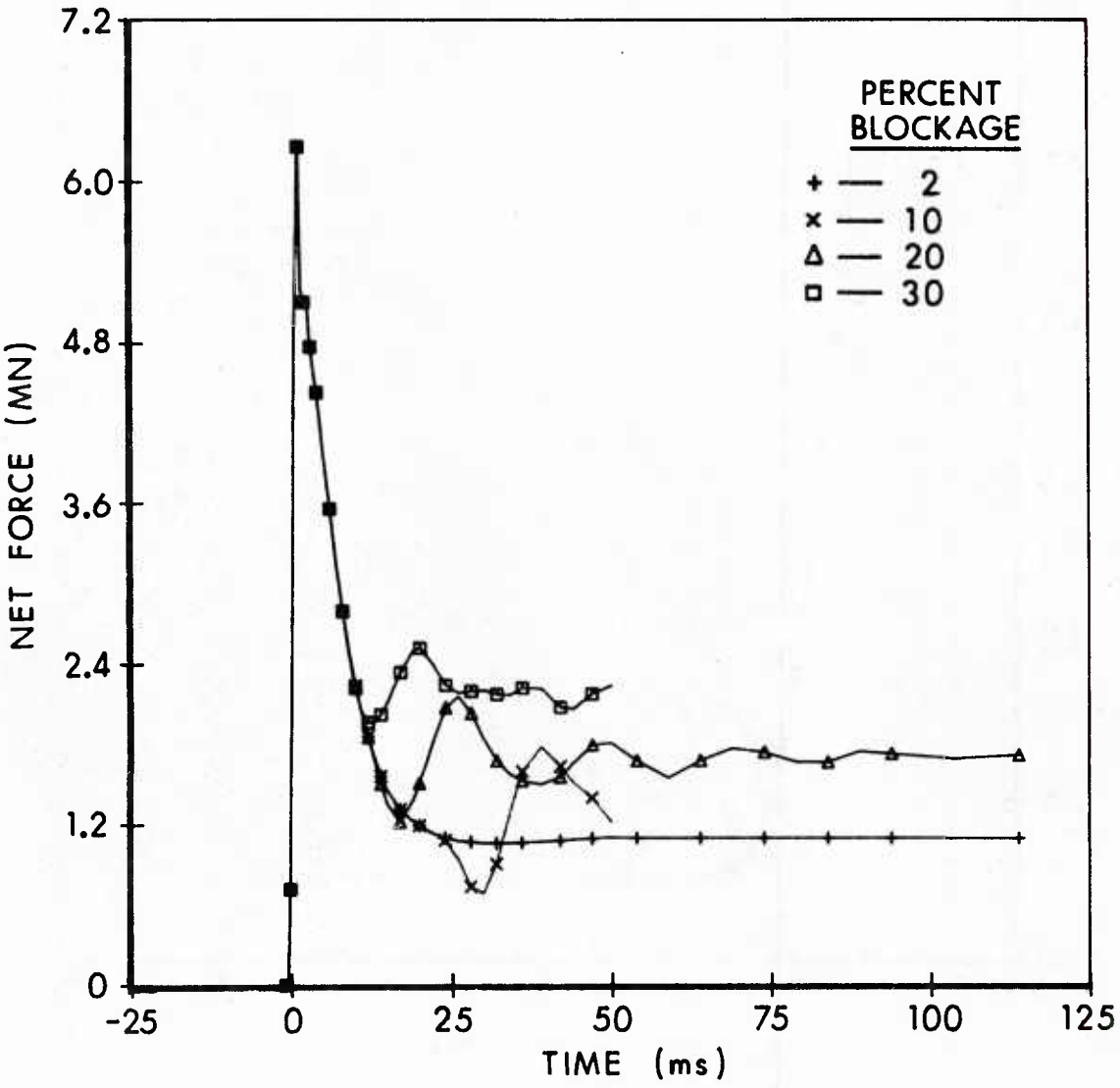

Figure 7. Net force on target cylinder for the 137.9 kPa shock.

percent blockage. In its simplest form, drag loading can be computed as the product of a drag coefficient and a dynamic pressure. The hydrocode computations showed that the trend of increasing dynamic pressure in the constricted-flow region with increasing blockage was qualitatively similar to the trend of increasing net axial force with increasing blockage. Therefore it seemed appropriate to use the dynamic pressure in the constricted-flow region from the hydrocode computations to develop a functional relation that could be used instead of hydrocode computations to predict changes in net axial loading due to blockage. The late-time values of dynamic pressure from each hydrocode computation were normalized by dividing by the free-field dynamic pressure behind the respective incident shocks. The resulting values of Q_R were then plotted versus B and found to be nearly independent from incident shock overpressure, except for the values for the 137.9 kPa shock at B=0.20 (small variation relative to other shock overpressures, onset of choking) and B=0.30 (large variation, choked). Accordingly, the results for the proportional increase in Q_R in the constricted region as a function of B were fitted to a formula, giving

$$Q_R = e^{\left(2.64B^{1.038}\right)} , \qquad (3)$$

with the data point for B=0.30 for the 137.9 kPa shock excluded.

The curve fit for Q_R versus B in Equation 3 provided a basis for calculating the dynamic pressure increase for a target in a shock tube relative to free field. The validity of this fit is limited to unchoked flow and late-time conditions for step shocks. The assumptions were made that the drag loading on a target could be calculated using a modified low velocity drag coefficient and the dynamic pressure increased by the factor calculated using Equation 3. This will be discussed in the section entitled "Application of Hydrocode Results."

This is an appropriate point in the discussion to explain the observed variations from the trend of Q_R versus B for B=0.20 and 0.30 for the 137.9 kPa overpressure shocks. Analysis of the computational results showed that the flows across the constricted-flow region (denoted by section line AB in Figure 4) for these cases were dominated by choking effects. The hydrocode results are supported by the results from the ideal nozzle computations shown in Figure 3. The limit for choking for an ideal nozzle for the late-time shocked air stagnation conditions for a 137.9 kPa overpressure shock corresponds to a value of B=0.177. This point is shown on Figure 3 as the connecting point between the subsonic flow curve for increasing Q_R with increasing B and the horizontal line for choked flow (i.e., Mach number unity) where Q_R is independent from B. The resulting point from the hydrocode computation for B=0.20 is well below this line. Analysis of the hydrocode results showed a large area within the constricted-flow region at a local Mach number near unity and a relatively low-velocity recirculation region. The results for B=0.30 showed a local Mach number near unity across nearly the whole region, with a much smaller recirculation region. This

explains why the hydrocode results for these two cases are low relative to the ideal predictions and the other hydrocode results for the same two blockages of B=0.20 and 0.30 and the other shock overpressures. The choking conditions place an upper limit on the dynamic pressure ratio, and the averaging with the lower-valued dynamic pressure ratios in the recirculation region further decreases the over-all value of Q_R. As may be seen in Figure 3, the values of Q_R from the hydrocode calculations agree very well with the ideal nozzle predictions for the other combinations of shock overpressure and blockage. This is largely because these cases are well below choking.

Figure 8 shows a set of normalized dynamic pressure histories for B=0.10, 0.20, and 0.30 for the 68.9 kPa overpressure step shock. These values were computed by taking average values across the center of the constricted-flow region (section lines AB for B=0.30, AC for B=0.20, and AD for B=0.10 in Figure 4) and dividing them by the dynamic pressure behind the undisturbed incident shock. A case with very low blockage would then show a normalized dynamic pressure very near unity for all time except during the early diffraction phase when velocities near the target are relatively high. Figure 8 shows a clear trend of increasing normalized dynamic pressure with increasing blockage. This typifies the results for the other shock overpressures of 34.5 kPa and 137.9 kPa (see Reference 2).

B. Decaying Shock Computations

A corresponding series of computations for rapidly-decaying shock waves having peak overpressures equal to the step shock overpressures was performed.[3] In that way, the two extremes of shock loading encounters could be documented. Hydrodynamic flow-field variables simulating a 0.1 KT* nuclear burst were produced by scaling from a curve fit for estimating free-field air blast based on a standard 1 KT nuclear burst.[4] Code modifications were made to utilize the variables computed by the fit for a radially divergent flow field to simulate a decaying planar shock wave in a tube. The planar decaying shock waves were produced by transforming the spherical shock wave from the LAMB coding into a planar wave in HULL by mapping sea-level flow-field variables from LAMB into HULL and using the velocity magnitude from LAMB for the axial component of velocity. The effective rotation of the velocity vector from a spherical coordinate system to a direction parallel to the axis of symmetry in a cylindrical coordinate system had the following effect. The transformation of the velocity vector from LAMB to the velocity vector in the shock tube is exact on the axis of the shock tube. (The axis is assumed to point toward the burst point.) At radial

Kiloton TNT, blast equivalent

[3] *J.D. Wortman and R.E. Lottero, "Comparison of HULL Hydrocode Computations of Shock Tube Blockage Effects on Target Loading for Step Shocks and Rapidly-Decaying Shocks," ARBRL-MR-03232, U.S. Army Ballistic Research Laboratory, Aberdeen Proving Ground, MD, December 1982. (AD A123274)*

[4] *C.E. Needham, M.L. Havens, and C.S. Knauth, "Nuclear Blast Standard (1 KT)," AFWL-TR-73-55(REV.), U.S. Air Force Weapons Laboratory, Kirtland Air Force Base, NM, April 1975. (AD#A014850)*

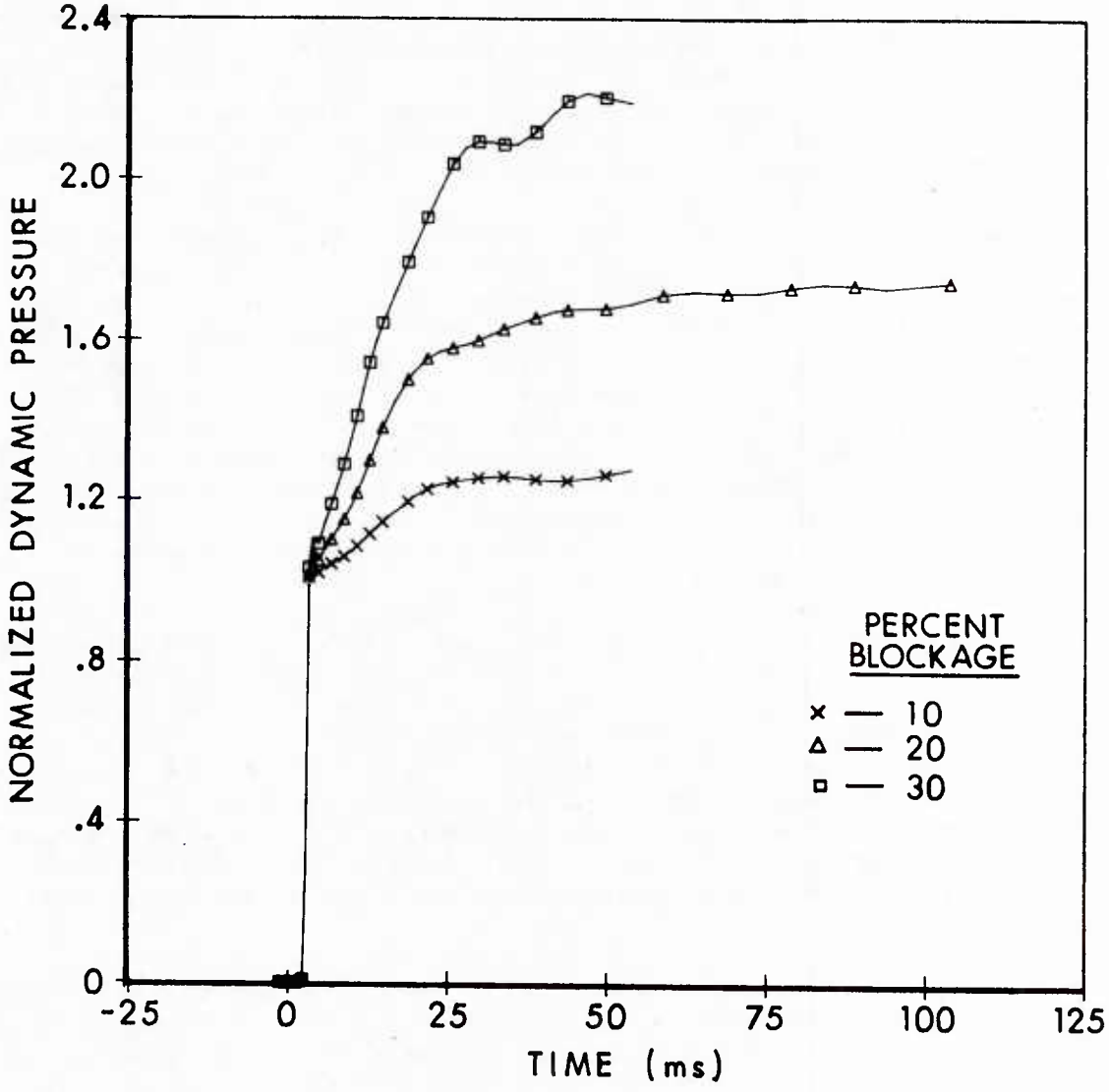

Figure 8. Average normalized dynamic pressure between cylinder surface and outer-radial boundary for the 68.9 kPa shock.

positions away from the axis, the LAMB velocity vector has two additional velocity components (if viewed in a three-dimensional Cartesian coordinate system). The "elimination" of these velocity components by this rotation of the vector caused increasingly larger "error" as the radial position in the shock tube increased. For a one percent blockage case, this error, at the entrance of the shock tube, ranged from 0 at the axis of symmetry to approximately 3.4 percent at the outer-radial boundary. The errors were less for the higher blockage computations. Once the computations were begun, the flow was constrained by the outer-radial boundary of the shock tube. This produced a shock wave which was different from that for a point-source blast wave because there was no further radial divergence in the shock tube.

Because the LAMB values for flow-field variables were computed from fitted curves, they are not necessarily self-consistent. Further, the velocity transformation used here produced some inconsistencies because the momentum equations in cylindrical coordinates do not contain the same radial divergence terms as in spherical coordinates. Once the HULL computation was begun, the input flow-field variables were used in the difference equations for cylindrical coordinates (with a no-outflow condition imposed at the outer-radial boundary) to compute mass, momentum, and energy transfer. This caused a set of perturbing waves to occur, further modifying the blast wave which was initially mapped into the computational grid. These inconsistencies did not have a significant effect on the computations; they are discussed more fully in Reference 3.

Calculations were made for decaying shock waves with peak overpressures (corresponding to the step shocks) of 34.5 kPa, 68.9 kPa, and 137.9 kPa. The approximate yield equivalence was 0.1 KT. This yield was chosen to provide nearly complete decay (of the 68.9 kPa shock) in the 100 ms time of interest, thus providing extreme cases for comparison with the step shocks. The target was identical to that used for the step shock waves. Computations were made for a nominal 20 percent blockage and also with the tube unobstructed to provide reference flow-field data. One run at 68.9 kPa was made for a very low blockage condition (B=0.01) to simulate essentially free-field conditions.

The histories of net axial force on the target for the 68.9 kPa shock computations are shown in Figure 9. The histories for the other shock strengths are similar. The diffraction loading phase is essentially unaffected by blockage because the reflected waves from the outer-radial boundary do not reach the target cylinder until very late in that phase. The two step shock curves are taken from Figure 6. They have been discussed in detail earlier, including their relation to curves for other values of blockage shown in that figure. Figure 9 typifies the relative differences between the results for step versus decaying shocks. It was chosen because the shock overpressure of 68.9 kPa and the blockage ratio B=0.20 each are mid-range values in the studies. Reference 4 contains a more detailed analysis of the decaying shock computations. However, a short discussion of the primary features of interest in Figure 9 is warranted here. There is agreement between all four curves through the early diffraction phase. This is so because the incident shock overpressures are the same and so is the reflection process. The curves then pair off, with the two curves for the decaying shocks showing more rapid pressure relief than the step shocks

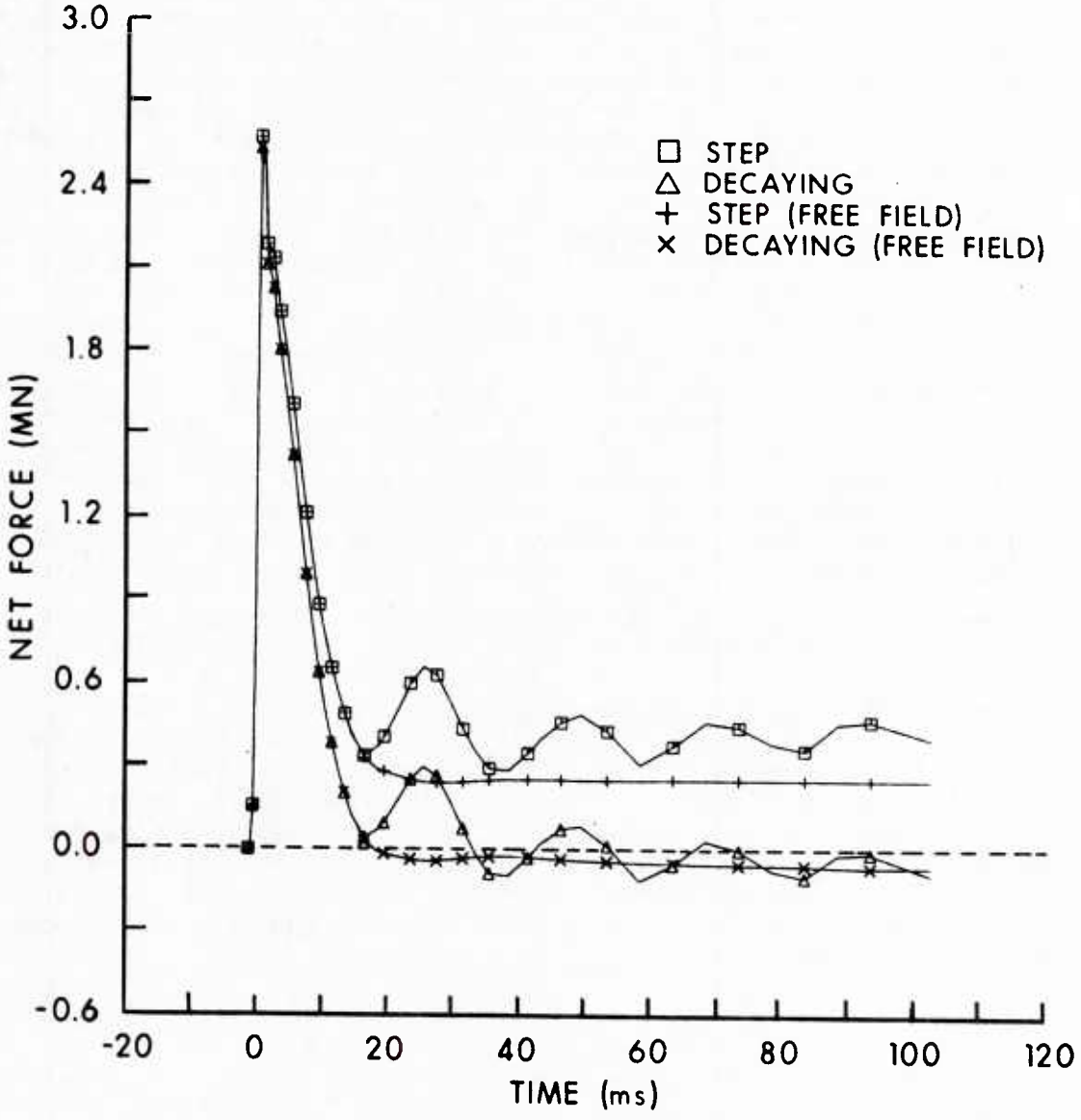

Figure 9. Comparison of net axial force on the target cylinder for step and decaying 68.9 kPa shocks with 20 percent blockage and with free-field conditions.

because of their overpressure decay. Both pairs of curves show essentially identical arrival times of the first reflected waves from the reflective outer-radial boundary. The free-field net axial force for the step shock quickly reaches a positive value of approximately 0.25 MN in its drag phase because of the steady flow behind the step shock. The free-field net axial force for the rapidly-decaying shock becomes negative at the end of the diffraction phase and remains negative for the duration of the computation. The negative net force for the decaying wave is due primarily to the rapid decay which produces a higher side-on overpressure in the plane of the back face of the target than at the front and acts counter to the force produced by air flow in the positive direction within the blast wave. The effect of the 20 percent blockage on the step shock is shown clearly in Figure 9; it has already been addressed in context with other blockage ratios in the discussion accompanying Figure 6. The effect of the 20 percent blockage relative to the free field results for the decaying shock is also evident in Figure 9. The net force oscillates about a value greater than that for the free field computation in the drag phase but about a value that is still negative. The frequencies of the oscillations are about the same for the step shock and the decaying shock. This is also true for the amplitudes of the oscillations, the exceptions to which are the 137.9 kPa step shock computations (discussed earlier and in Reference 3 in detail) where choking conditions exist in the constricted-flow region. Overall, the net axial force in the drag phase for this rapidly-decaying shock appears to be relatively unimportant, both for the free field case and for B=0.20, especially compared to that for the step shock. These results typify those for the other comparisons[3] between step and rapidly-decaying shocks at overpressures of 34.5 kPa and 137.9 kPa, except as noted above.

Figure 10 shows the average dynamic pressure across the line of cells (denoted by section line AC in Figure 4) in the center of the constricted region for the 68.9 kPa shock waves. The plots for the other shock strengths (see Reference 3) are similar. In addition to the dynamic pressures for the 20 percent blockage case, the figure includes the dynamic pressure for the decaying shock in an empty tube. This begins with a peak value and decreases smoothly toward zero. The corresponding dynamic pressure for a step shock in an empty tube is a step function which jumps from zero to a constant value.

Figure 11 shows the relative effect of blockage on the normalized average dynamic pressure in the constricted region for the 68.9 kPa step shock and the corresponding decaying shock wave. The set of normalized average dynamic pressure curves for B=0.10, 0.20, and 0.30 for the step shock has already been shown in Figure 8 and discussed. The average dynamic pressure for the 68.9 kPa step shock is normalized by dividing by the dynamic pressure (15.27 kPa) behind the incident shock prior to its interaction with the target. The dynamic pressure of the decaying wave when blockage was simulated was normalized by dividing by the corresponding dynamic pressure at that time from the empty tube computation. The increase in normalized dynamic pressure is greater in a relative sense for the decaying shock than for the step shock for 68.9 kPa overpressure and B=0.20. This was true of the other shock overpressures as well.[3] However, because the dynamic pressures for both free field and blockage computations become

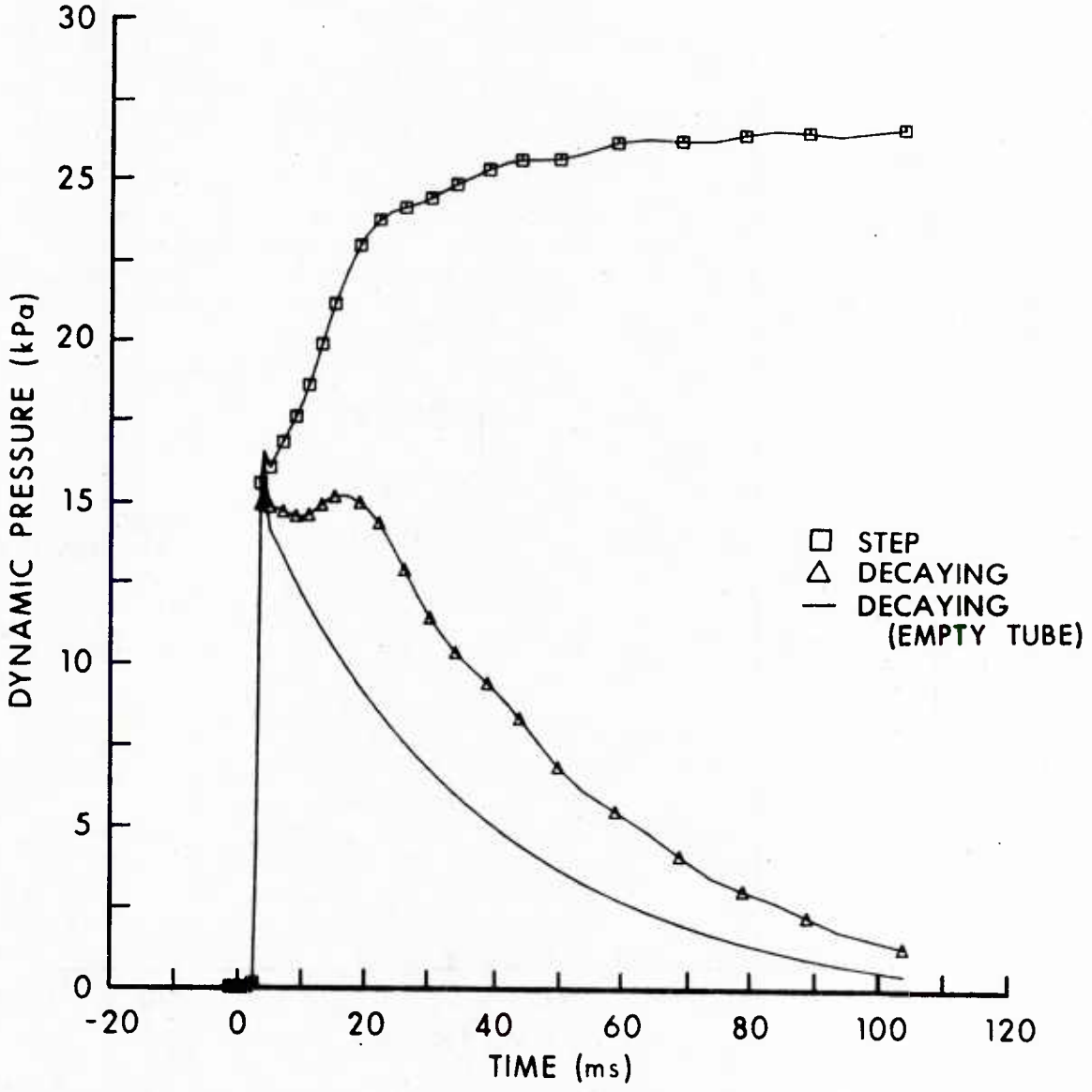

Figure 10. Average dynamic pressure between the target cylinder and the outer boundary for 68.9 kPa shocks with 20 percent blockage.

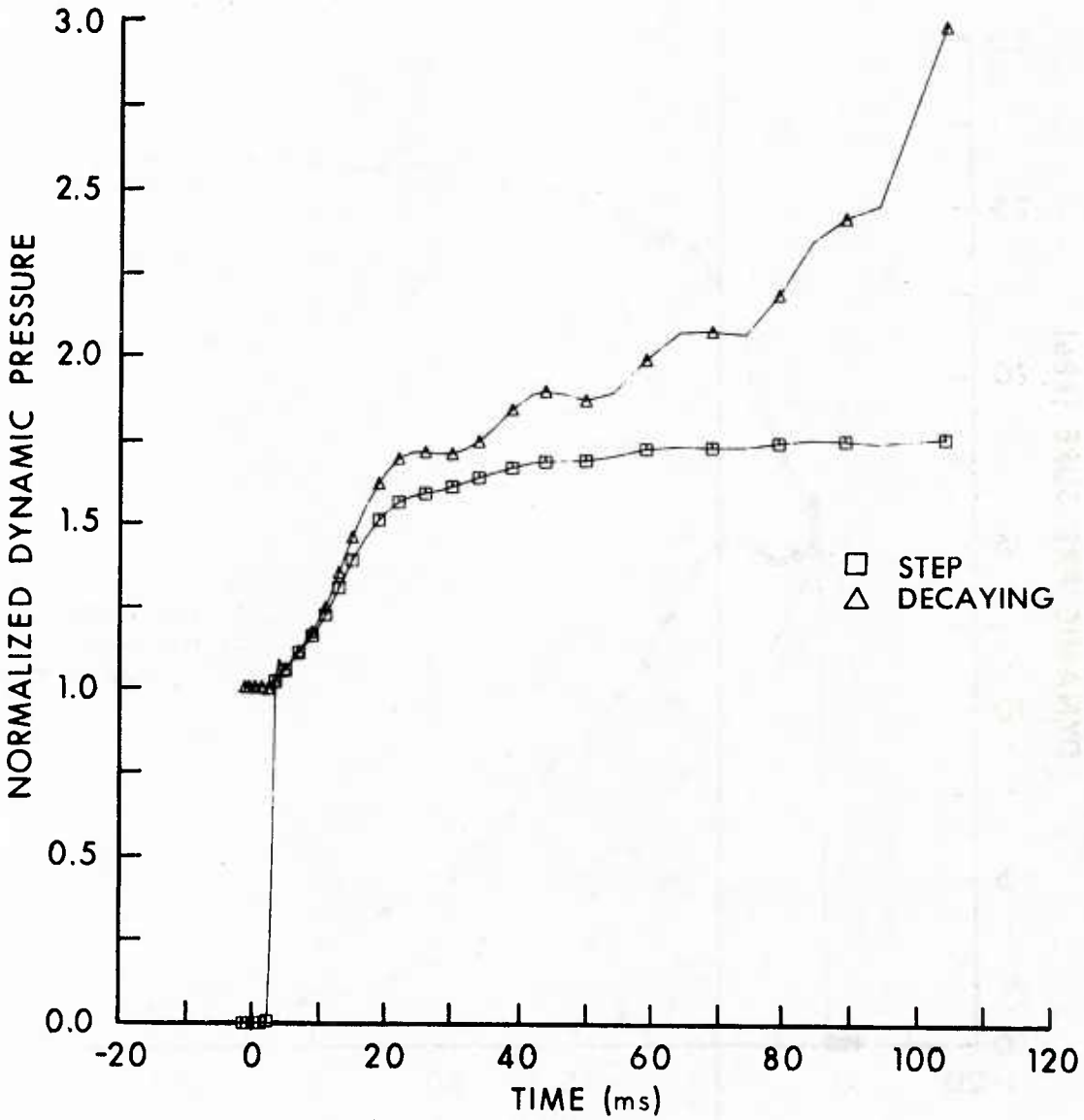

Figure 11. Normalized average dynamic pressure between the target and the outer boundary for 68.9 kPa shocks with 20 percent blockage.

small at late time, less confidence must be placed in their ratios. The late-time normalized values are included in Figure 11 to illustrate this effect.

IV. APPLICATION OF HYDROCODE RESULTS

A single degree of freedom (rotation only) computer code called BLOM[5] (Blast Overturning Model) was used to model the effect of blockage on the overturning of vehicles. In addition to containing a diffraction loading model, the code is also capable of performing drag loading calculations. The drag loading is calculated as the product of a drag coefficient CD, the presented area, a function accounting for the change in presented area with changing angle of inclination as the target rotates, and the dynamic pressure. The drag coefficient is expressed as a product of CD_o, the effective low-velocity drag coefficient, and a function which is unity at low velocity and increases with local Mach number. Equation 3 was used to compute the change in dynamic pressure not only due to the initial blockage, but also due to the changed blockage as the target rotates. This procedure was used to predict the change caused by blockage in the minimum incident shock overpressure required to overturn three representative tactical vehicles. The results showed a significant decrease in the minimum overpressure required for overturning as blockage is increased. Decaying waves with corresponding peak overpressures for a range of yields from 3 to 1000 KT were used. The results showed relatively little dependence on yield. The use of Equation 3 to calculate estimates for increases in dynamic pressure in the constricted-flow region due to blockage for decaying shocks represented an extrapolation beyond its established applicability.[2] The question arose as to the validity of applying predictions based on non-decaying shock wave results to the more realistic decaying waves modeled in large blast simulators.

The function listed as Equation 3, which describes the enhancement of dynamic pressure with blockage ratio for step shocks, predicted the magnitude of increase in a marginally satisfactory manner at the beginning of the drag phase for the rapidly-decaying wave and became increasingly worse as time progressed. In its present form, its utility is limited to step and slowly decaying shock waves.

For decaying waves, the importance of blockage effects depends upon the relative proportion of the net loading in the drag phase compared to that in the diffraction phase. For the extreme case of a yield equivalent of 0.1 KT and for the range of shock overpressures and blockages considered in the study, blockage effects were not important for determining the net axial loading.

---

[5] *N.H. Ethridge, "Blast Overturning Model for Ground Targets," Proceedings of the Fourth International Symposium on Military Applications of Blast Simulation, Southend-on-Sea, England, September 9-12, 1974.*

V. FLOW CONTOURS AROUND THE TARGET IN THE HULL COMPUTATIONS

Figure 12 shows the iso-value contours for the dynamic pressure ratio around the cylindrical target that were derived from the HULL calculations for the series of step shocks at 20 percent blockage. The normalizing dynamic pressure was that immediately behind the incident shock front. The incident shock wave entered from the right. Times ranged from 0.095 to 0.12 seconds to obtain contours at late times and at about the same number of shock crossing times.

A region with an increase of more than a factor of two in Q_R is shown in the flow fields. It is located progressively farther downstream as the shock overpressure is increased. Despite the shift in flow contours, the average dynamic pressure ratio radially across the cells at the center of the constricted region was 1.65 for the 34.5 kPa shocks, 1.69 for 68.9 kPa, and 1.60 for 137.9 kPa. The average of these is 1.65, with a variation of $\pm$ 3 percent. This lack of variation of Q_R was exploited to generate Equation 3. Figure 13 shows the contours for local Mach number for the step shocks. For the 137.9 kPa shock the maximum Mach number noted in the field was 0.98, confirming the essentially choked condition of the flow.

Figure 14 shows contours of dynamic pressure ratio for the step shocks at 2 percent blockage, essentially a free-field condition. Here the maximum Q_R is 1.57 for the 34.5 kPa shock and 1.44 for the 137.9 kPa shock. The region of maximum Q_R elongates at 137.9 kPa but shifts downstream only slightly, in contrast to the large shift that occurs for 20 percent blockage. The contour patterns are similar for all three overpressures.

The contour plots of dynamic pressure ratio and Mach number show that gages measuring dynamic pressure or particle velocity would record very different values depending upon their location in the flow field with respect to the target. Figure 15 presents dynamic pressure, Mach number, particle velocity, density, and overpressure normalized by the values behind the incident step shock along a line parallel to the axis of the shock tube and 0.83 metres from the wall for 20 percent blockage. The front face of the target is at 0.0 and the shock wave moves in the positive direction. The dynamic pressure is the parameter most sensitive to position along the line. Within 0.2 target lengths in front of the leading edge of the target, the change in Q_R would range from about 10 percent at 137.9 kPa to 50 percent at 34.5 kPa. An examination of differential pressure gage records made about one metre from the wall and slightly in front of a truck-shelter target in the blast simulator at Centre d´Etudes de Gramat, Gramat,

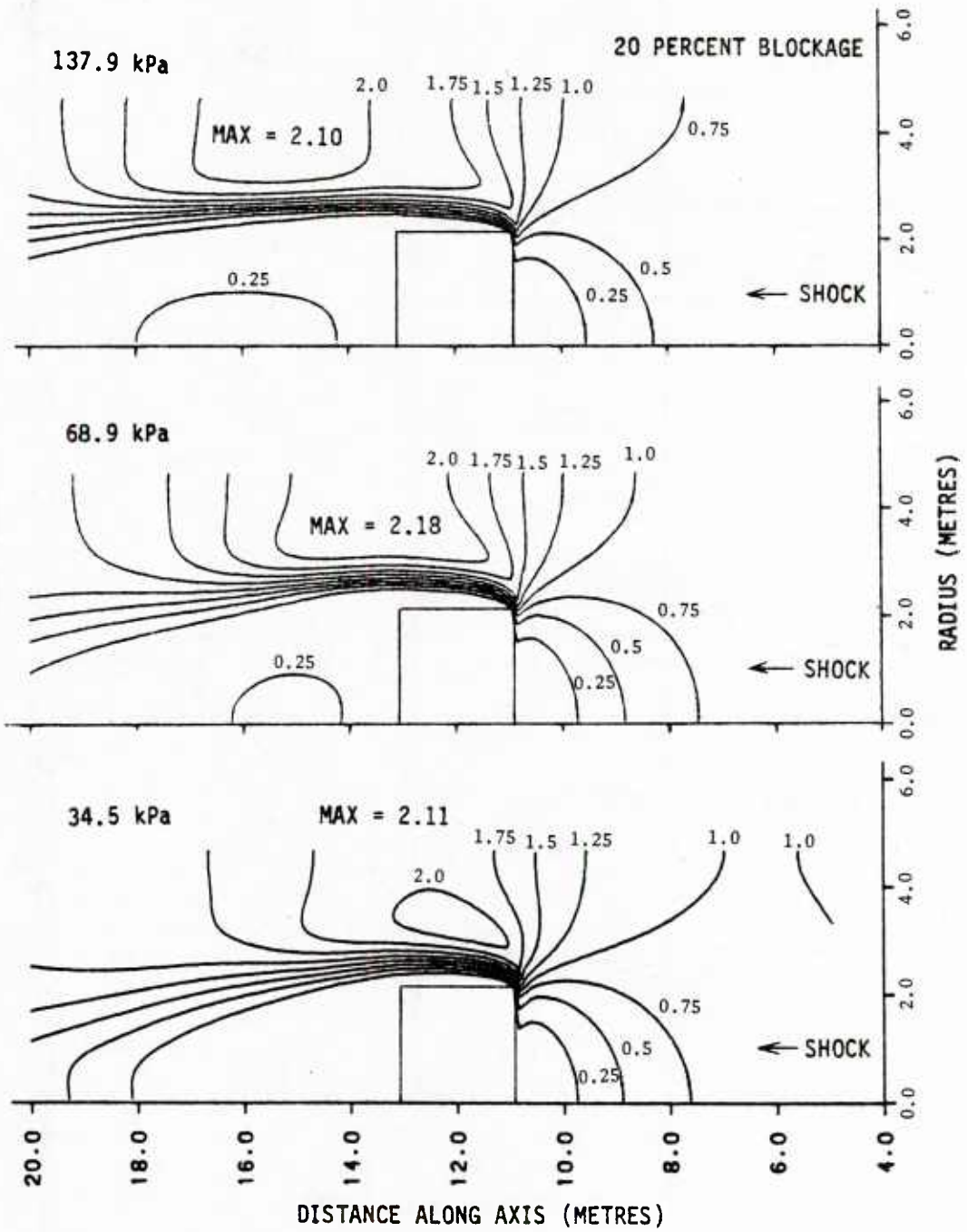

Figure 12. Iso-value contours of dynamic pressure ratio around the HULL target for step shocks at 20 percent blockage. The normalizing value was that immediately behind the shock front.

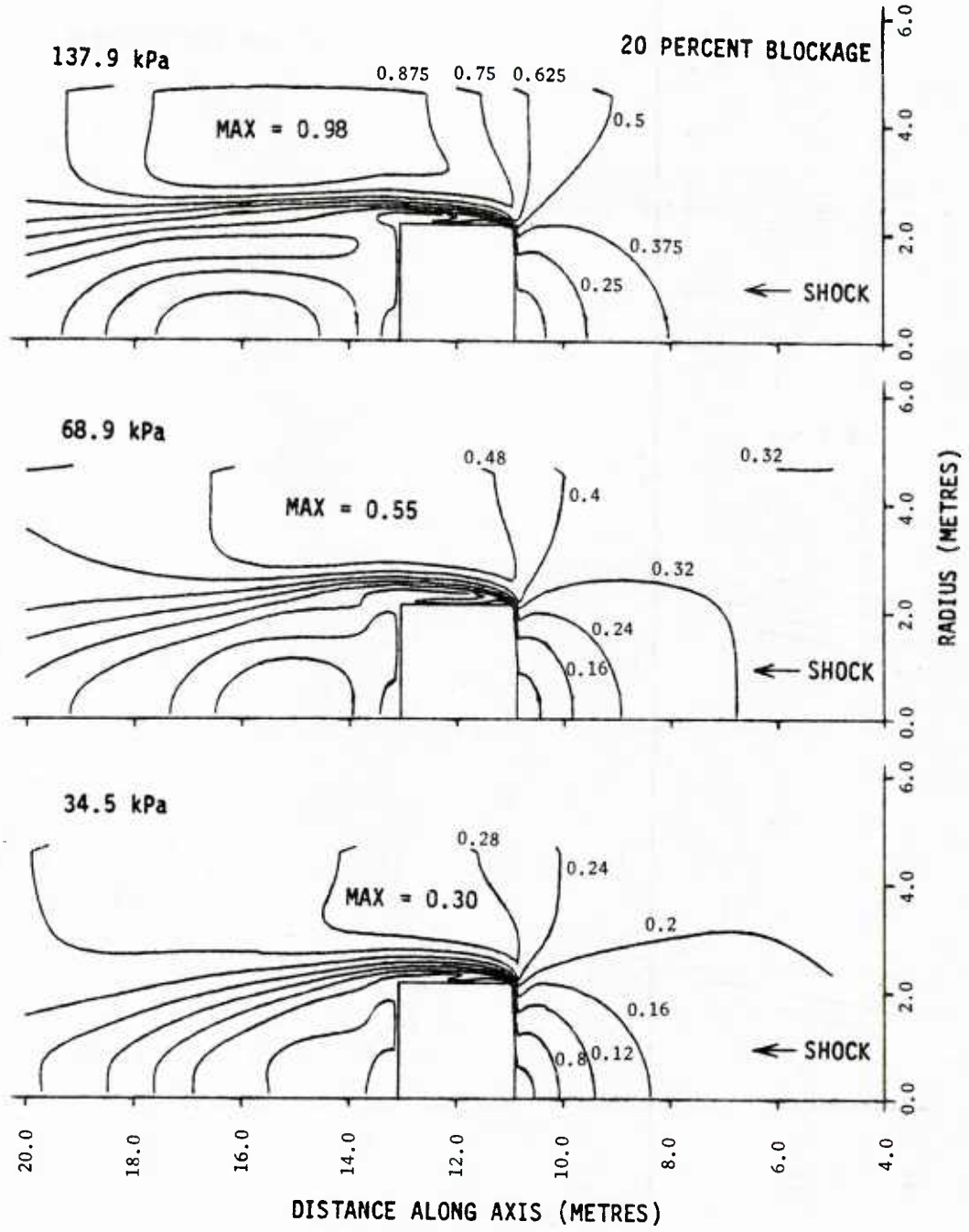

Figure 13. Iso-value contours of local Mach number around the HULL target for step shocks at 20 percent blockage.

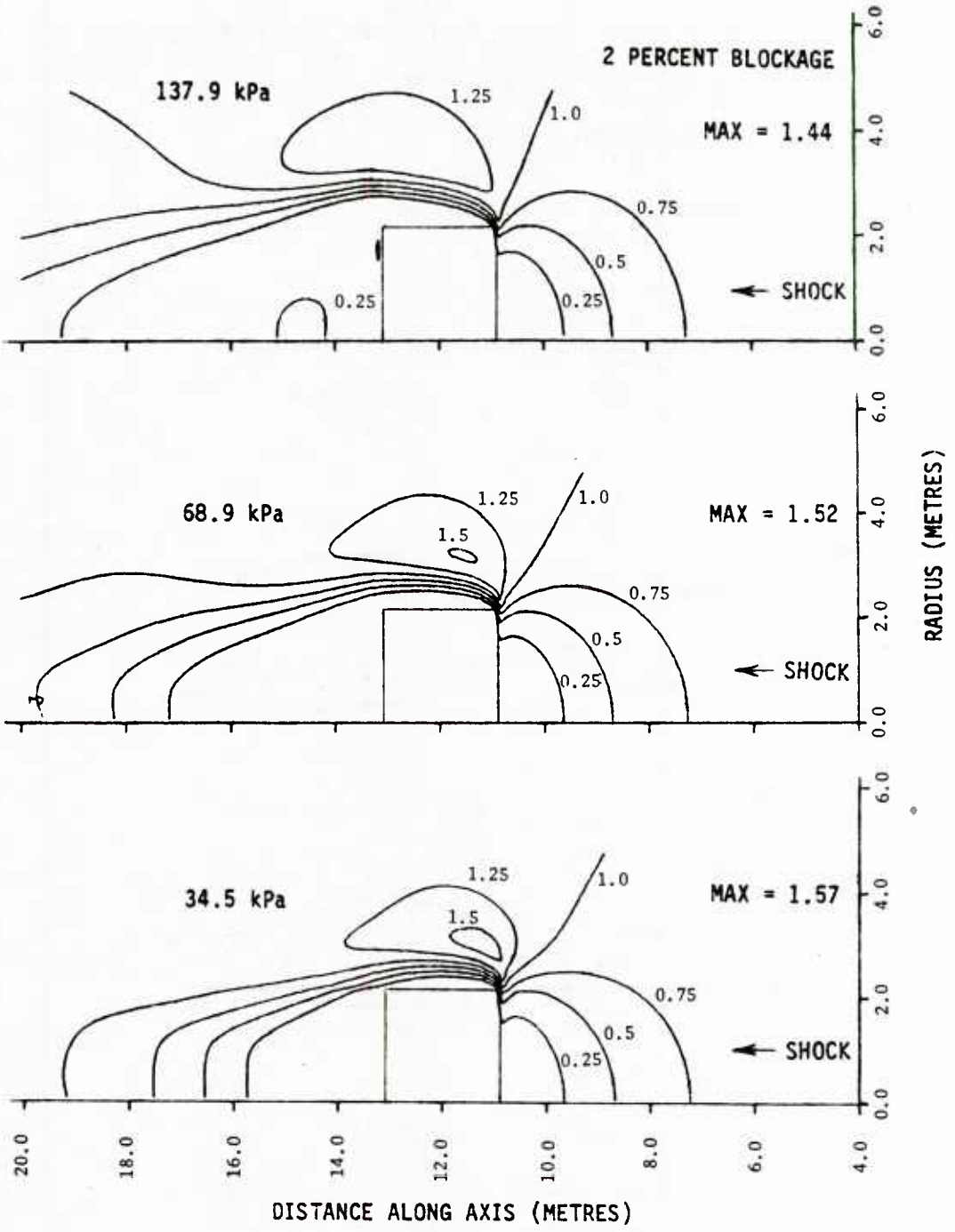

Figure 14. Iso-value contours of dynamic pressure ratio around the HULL target for step shocks at 2 percent blockage.

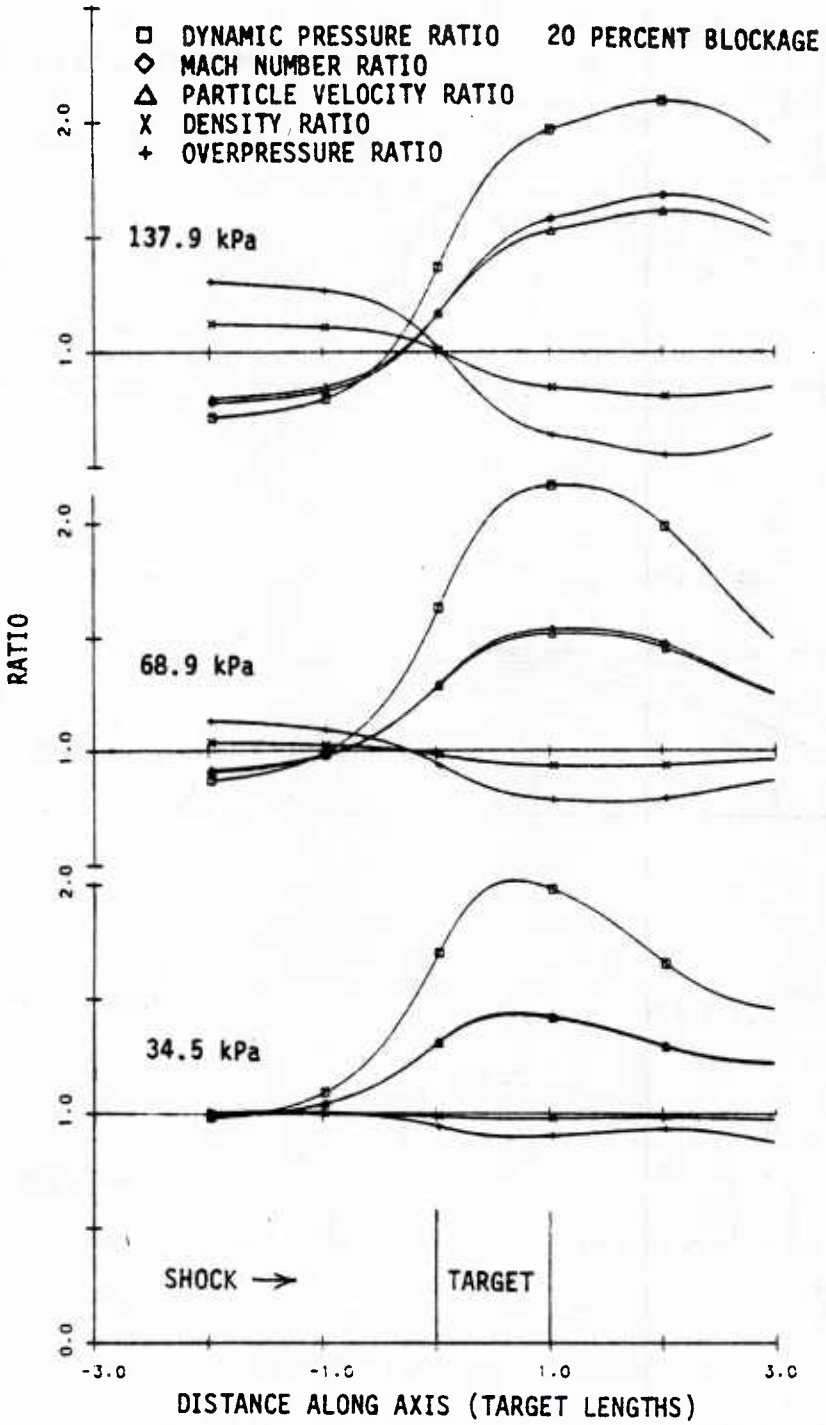

Figure 15. Ratio of flow variables along line parallel to axis and 0.83 metres from wall at 20 percent blockage to values behind incident step shock.

France,[6,7] and at the same position with the test section empty for the same incident shock strength showed an increase with the target present which is in reasonable agreement with the HULL results.

This sensitivity of gage readings to position should be considered in the design of the simulator instrumentation layout and in the interpretation of the gage measurements. The problem of interpretation of the gage readings becomes even more complicated if the target moves during blast loading.

VI. FORCE ON SIDE OF TARGET IN THE HULL COMPUTATIONS

In the previous study[2] the HULL computations were analyzed to derive the net axial force, and as stated previously, the results showed no significant effect due to blockage until late in the diffraction phase for $B \geq 0.2$ and no effect in the diffraction phase for $B < 0.2$. Situations may arise during the testing of a target where reflected waves from the shock tube walls may cause side and top walls to be loaded to levels greater than expected for a free-field interaction with the same blast wave. If so, wall deflections may occur where none would normally be expected, or deflections may be greater than expected. The hydrocode computations may also be used to estimate the changes in side face loading. The computations for the step shocks were processed to derive the average overpressure versus time on the sides of the cylindrical target. Figure 16 shows the average overpressure on the target side face versus time for the range of shock overpressures and blockages computed. Zero time corresponds to the arrival of the shock front at the front face of the target. The 2 percent blockage case corresponds to free-field conditions. For blockages of 10, 20, and 30 percent, a large second peak in the target side-loading is generated by the return to the target side of waves reflected from the walls of the shock tube. For 30 percent blockage, the second maximum is larger than that of the initial peak loading. The time for achieving peak wall deflection of a target such as a communications shelter is in the range of 0.005 to 0.008 seconds. At 10 and 20 percent blockage, the time separation of the second peak from the first seems sufficient to not interfere with the maximum deflection generated by the first peak, although additional damage may be produced by the second pulse. For 30 percent blockage, however, the peaks are merged to the extent that the wall response might not be the same as that produced under free-field conditions.

---

[6] *J.R. Crosnier and J.B. Monzac, "Large Diameter High Performance Blast Simulator," Proceedings of the Fifth International Symposium on Military Applications of Blast Simulation, Stockholm, Sweden, May 23-26, 1977.*

[7] *J.R. Crosnier, S. Gratias, J.B. Monzac, and H. Richard, "Concepts and Design for a Large Diameter High Performance Blast Simulator," Proceedings of the Fourth International Symposium on Military Applications of Blast Simulation, Southend-on-Sea, England, September 9-12, 1974.*

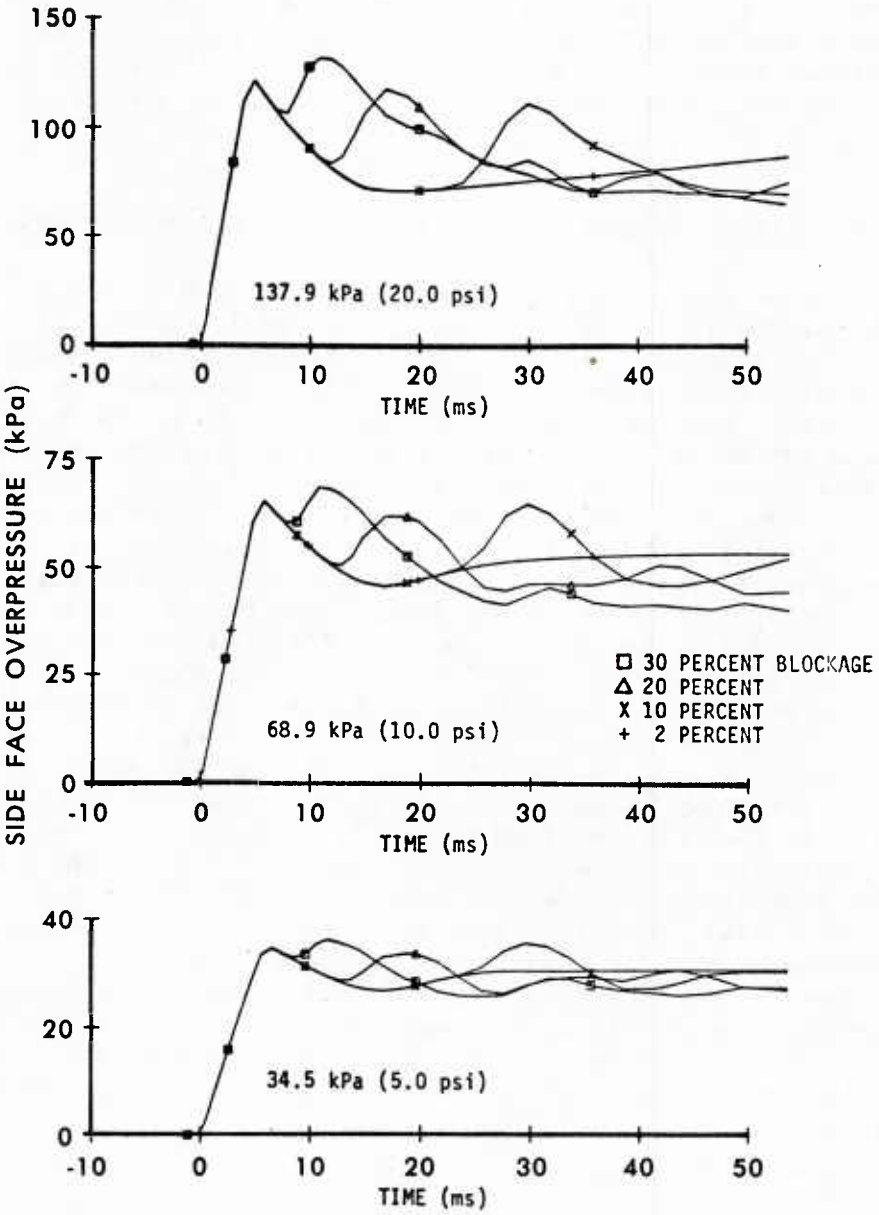

Figure 16. Average side face overpressure on the target cylinder for step shock overpressures of 34.5, 68.9, and 137.9 kPa.

VII. SHOCK TUBE EXPERIMENTS

A series of experiments were conducted using the BRL 0.56 metre diameter shock tube[8] to measure the drag force on cylinders of the same length to diameter ratio used for the target in the HULL calculations. The cylinders were hung in the center of the shock tube with their axes parallel to that of the tube. The procedure was to suspend the cylinders so that they were free to translate and to derive the drag force produced by the non-decaying portion of the incident shock wave from the observed displacement versus time along the axis of the shock tube. Different diameter cylinders were used to produce different blockage ratios. The masses were varied to control the amount of displacement produced in the observation time of interest. Table 1 lists the target characteristics, the measured shock overpressures and corresponding calculated dynamic pressures, and derived drag force per unit area.

Figure 17 shows the test layout. The test section had a square cross-section with an area of 0.258 square metres. The cylinders were suspended by two support wires that were attached to a frame that was independent from the shock tube. The wires entered the test section through slots in the top of the tube. The slots were 13mm long to permit the cylinders to swing through the range of measurement (0 to 0.05 metres) without the wires making contact with the shock tube structure.

The movement of the cylinder was measured by an elecro-optical displacement follower, an instrument which generates a signal related to the movement of a high-contrast boundary across its field of view. Each cylinder was painted on the side with a black and a white stripe to produce a high contrast boundary in the center of its side. For calibration the cylinders were suspended in place, displaced by known distances, and the output of the displacement follower recorded. The drag force on the suspension wires and the pendulum resistance force were negligible compared to the drag force acting on each cylinder.

The assumption made in designing the experiment was that for an incident non-decaying shock wave the drag loading on the target would be constant after the end of the diffraction loading period, with the exception of a small decrease caused by the decrease in relative air velocity with time as the target accelerated. The portion of the recorded motion used was selected to be well after the initial diffraction loading period but before the velocity of the cylinder became significant and ranged from about 0.006 to 0.032 seconds, depending upon the particular cylinder and the shock overpressure.

---

[8] *G.A. Coulter and B.P. Bertrand, "BRL Shock Tube Facility for the Simulation of Air Blast Effects," US Army Ballistic Research Laboratory Memorandum Report No. 1685, August 1965. (AD#475669)*

TABLE 1. SHOCK TUBE FREE-FLIGHT CONDITIONS AND RESULTS

Shot No.	Mass (kg)	Diameter (m)	Length (m)	Blockage Ratio	Measured Overps (kPa)	Calculated Dynpress (kPa)	Derived Drag F/A (kPa)
81-161	0.510	0.0762	0.0386	0.0177	35.0	4.02	4.8
81-160	0.510	0.0762	0.0386	0.0177	71.1	16.02	20.0
82- 01	1.397	0.0762	0.0386	0.0177	97.9	29.24	38
82- 02	1.397	0.0762	0.0386	0.0177	135.1	53.44	71
81- 67	4.400	0.2606	0.1316	0.2067	35.0	4.05	8.3
81- 71	4.400	0.2604	0.1308	0.2063	68.5	15.03	33
81-148	13.263	0.2606	0.1318	0.2067	137.4	54.88	129
81-149	5.534	0.3175	0.1610	0.3068	37.0	4.52	10.7
81-152	5.352	0.3175	0.1610	0.3068	72.2	16.71	36
81-154	14.742	0.3175	0.1610	0.3068	102.3	32.34	79
81-153	27.329	0.3175	0.1610	0.3068	138.6	56.74	133

Overps = incident shock overpressure.

Dynpress = dynamic pressure behind the shock front calculated from overps.

F/A = translational force per unit area acting on the cylinder.

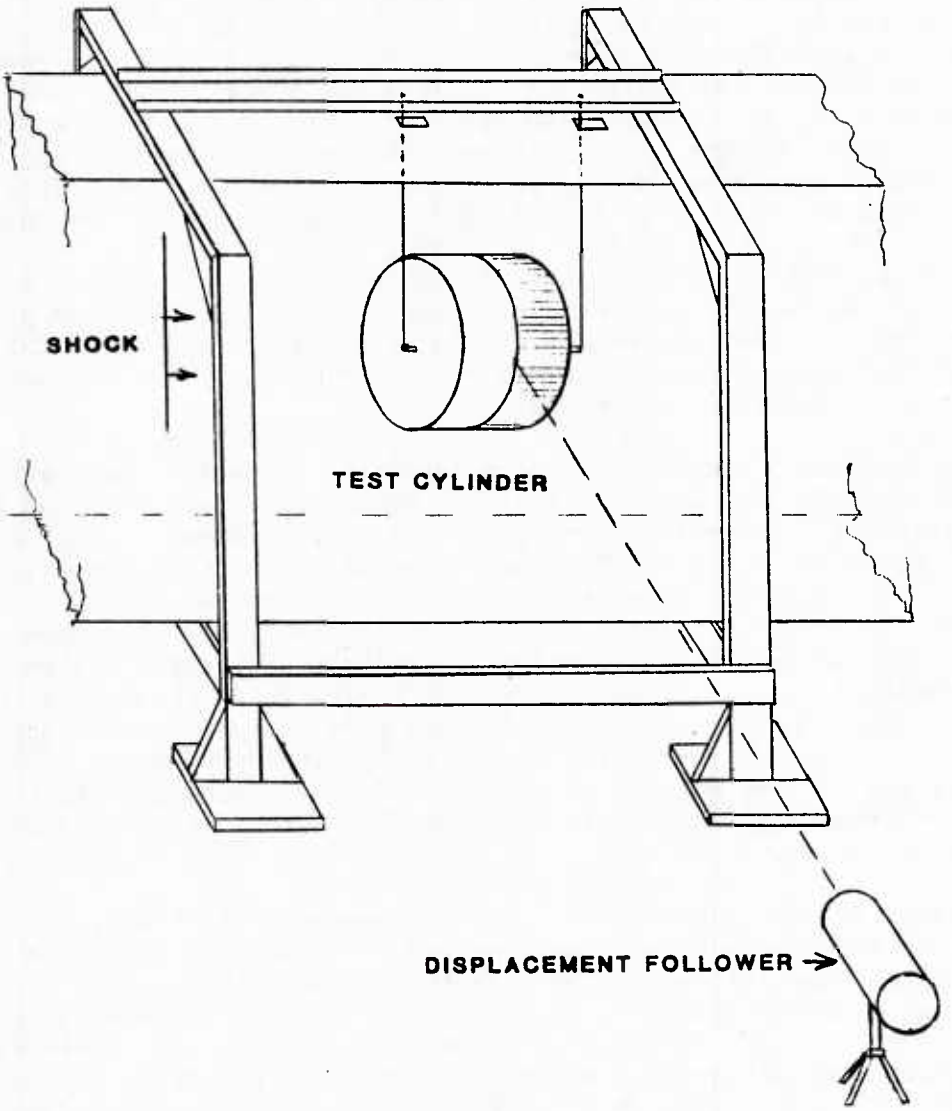

Figure 17. Layout for shock tube tests.

For cylinder loading occurring as expected, if M is cylinder mass, x is displacement, and t is time afer shock arrival, the ratio 2Mx/t when plotted against t is approximately a straight line (i.e., constant acceleration) in the time period of interest. The positive intercept on the 2Mx/t axis is related to the impulse delivered during the diffraction loading period, and the slope of the line is the drag force of interest. Figure 18 shows a record of displacement versus time for shot 81-148, and Figure 19 shows the corresponding plot of 2Mx/t versus t. A line was fitted through the data by least squares over the selected time span, and the slope and hence drag force was derived from the fit. This procedure was followed for all shots. The results were converted to drag force per unit area and are listed in the last column of Table 1. The estimated error range is $\pm$ 10 percent.

Table 2 lists the estimated late-time drag force per unit area for the HULL calculations for the step shock. Because of the oscillations present in the net force curves, the most reliable values are for the 0.21633 blockage ratio, where the calculations were carried to a time of about 0.1 seconds, rather than to 0.05 seconds.

Figure 20 shows a comparison of the late-time net axial force per unit area on the cylinders as derived from the shock tube experiments and the HULL computations. Power law least squares fits were made for each set of data for a particular percent blockage. The solid lines are the fits to the HULL data, and the dashed lines are for the shock tube results. The upper dashed curve is for 30 percent blockage, and the lower for 20 percent blockage. At 2 percent blockage the fits for both HULL and the experiments agree to within $\pm$ 3 percent, and hence only one curve is shown. At 20 percent blockage, the shock tube results are from 5 to 10 percent above those of HULL, although the difference is within the error range of the experiments and the estimations of the late-time net force from HULL plots. At 30 percent blockage the HULL results are from 7 to 22 percent above those from the experiments.

The reason for these differences is not known at this time. The cross-section of the shock tube test section was square, rather than round as in the HULL computations, so that may be a contributing factor. Small changes in geometry or flow parameters for nearly choked flow will cause relatively large changes in results in both computations and experiments. Viscous effects are not modeled in HULL, so viscous drag force is absent from the HULL results. Also, HULL probably gives less accurate results for use in computing loading on the back face than on the front face. Nonetheless, the shock tube experiments confirmed that large increases in axial loading occur at blockages of 20 and 30 percent and that the HULL hydrocode predicted the increase reasonably well.

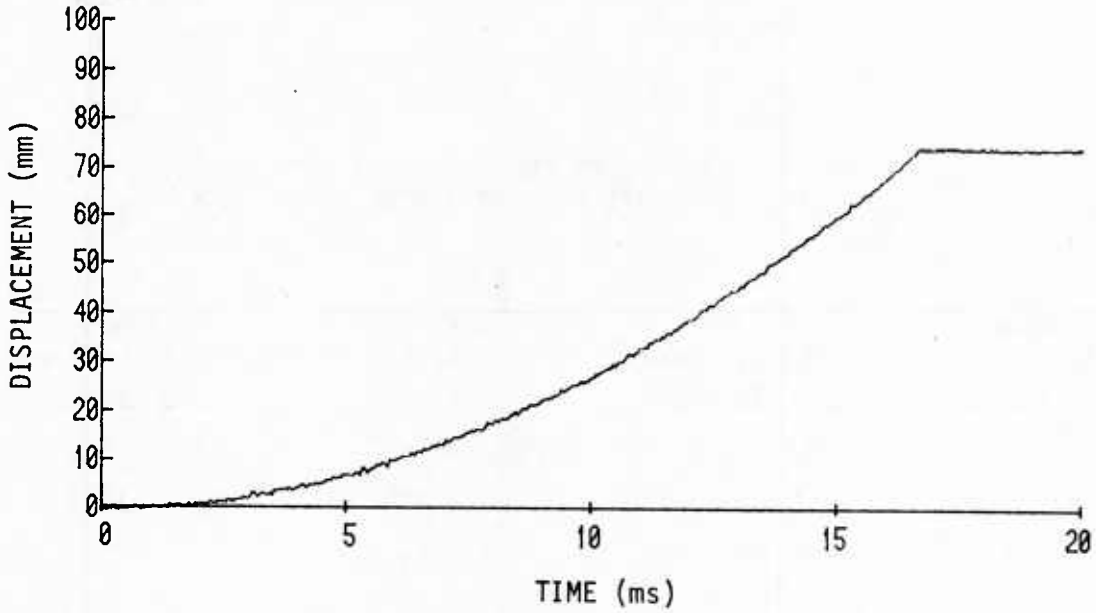

Figure 18. Displacement versus time for shot 81-148 at a shock overpressure of 137.4 kPa.

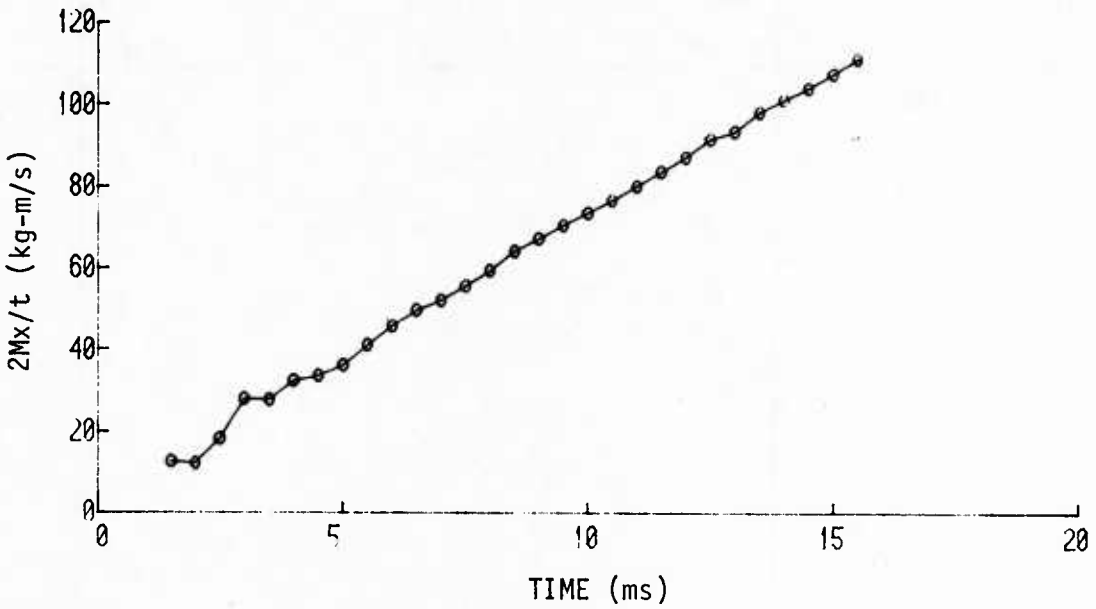

Figure 19. Data from shot 81-148 plotted for measuring slope of line and drag force per unit area.

TABLE 2. DRAG FORCE PER UNIT AREA FROM THE HULL COMPUTATIONS FOR A STEP SHOCK WAVE

Blockage Ratio	Shock Overpressure (kPa)	Dynamic Pressure (kPa)	Drag Force/Area (kPa)
0.02020	34.5	4.00	5.0
0.02020	68.9	15.27	17.2
0.02020	137.9	56.11	76
0.21633	34.5	4.00	7.6
0.21633	68.9	15.27	31.0
0.21633	137.9	56.11	118
0.32653	34.5	4.00	11.0
0.32653	68.9	15.27	39.3
0.32653	137.9	56.11	150

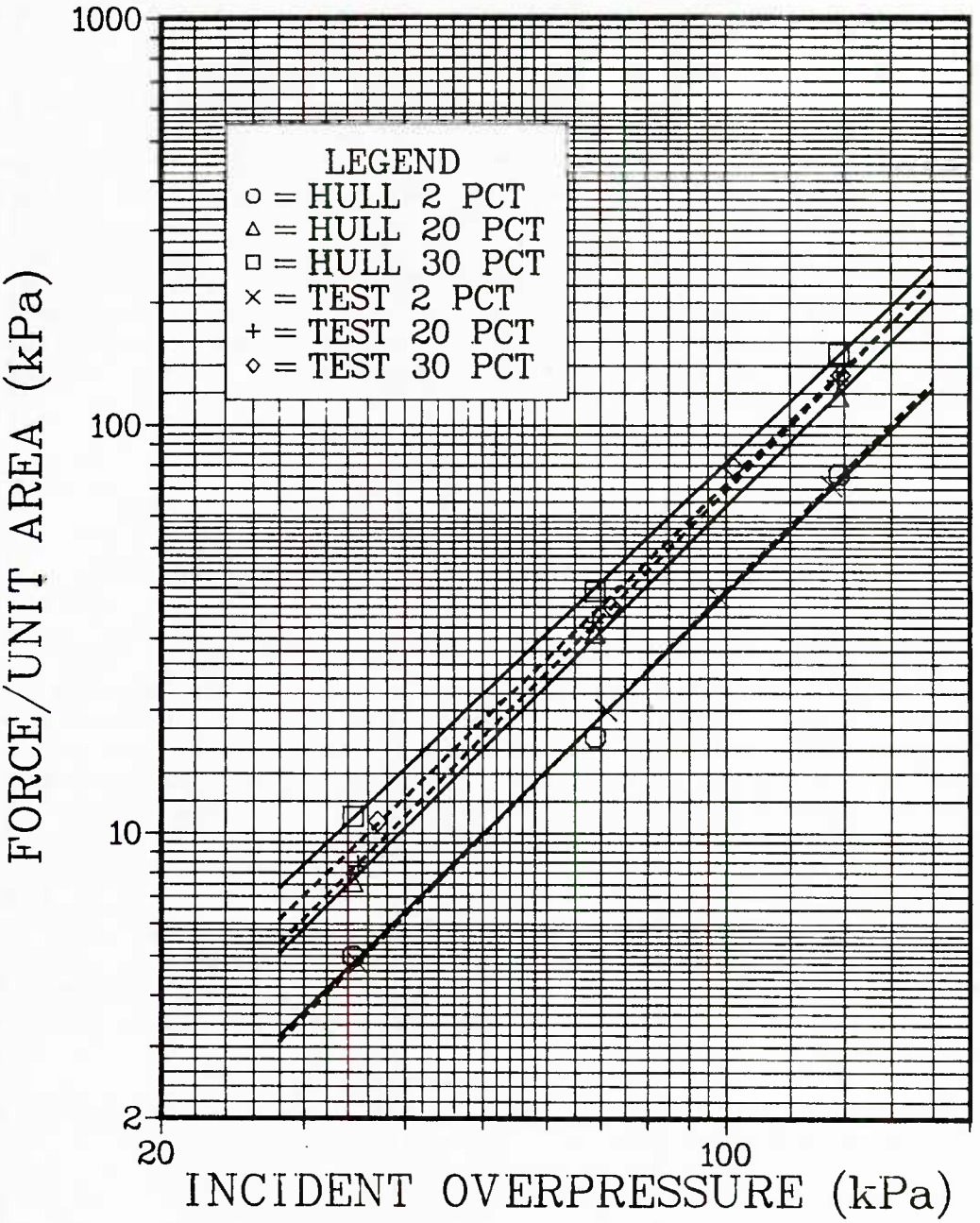

Figure 20. Comparison of late-time net axial force per unit area for cylinders derived from HULL computations and shock tube experiments versus incident shock overpressure for blockages of 2, 20, and 30 percent. The solid lines are power law least squares fits to HULL data, and the dashed lines are fits to shock tube experimental data.

VIII. COMPARISON OF HULL DRAG PHASE LOADING WITH WIND TUNNEL DATA

In Reference 9 a study was made of blockage corrections for bluff body models which approximate road vehicles. Tests with models were made in a wind tunnel with a test section 0.76 m by 0.60 m and 3.6 m long and a maximum particle velocity of 16 metres/second. The models were rectangular parallelepipeds of square cross-section, with a length to width ratio of 2.5, and were supported near the floor with the length parallel to the direction of air flow. The models were sized to produce blockages up to 15 percent. An initial study was made of the pressure distribution on the models, and it was shown to be invariant with blockage.* A blockage correction factor was determined empirically that was judged to be valid for blockages up to 20 percent for such bluff bodies. The correction factor was of the following form:

$$1/f = 1/(1 - mB) \tag{4}$$

where: f = blockage correction factor = $1/Q_R$

m = 1.9, a constant determined from the above experiments. It is generally dependent on drag coefficient, body shape, and test section geometry.

A comparison of the results from HULL for the step shocks shows that Equation 4 with m = 1.9 agrees well with HULL data for cylindrical models and with Equation 3 fitted to the HULL data. The value of m derived from the shock tube translation experiments is 2.2 for 20 percent blockage. The target in HULL and in the shock tube experiments had a length to width ratio of about 0.5, while that of the wind tunnel models was 2.5. The wind tunnel tests were made at very low velocities compared to those that occurred in the HULL computations and shock tube experiments. The wind tunnel tests also included ground effects on the model which were not present in either the computations or the shock tube experiments. The targets in all cases had sharp corners. The agreement may be fortuitious, but the values of m derived from HULL and the shock tube experiments are compatible with the wind tunnel data.

Another correction factor discussed in Reference 9 is one derived from conservation of mass flow, and is as follows:

$$1/f = 1/(1 - B)^2 \tag{5}$$

The lack of variation may have been due to the low local Mach number of the incident flow.

[9] *D.M. Sykes, "Blockage Corrections for Large Bluff Bodies in Wind Tunnels," Paper 18, Advances in Road Vehicle Aerodynamics, Edited by H.S. Stevens, BHRA FLuid Engineering, pp 311-322.*

It has no provision for variation with body shape or other factors. This relation describes the curve that would be plotted in Figure 3 for the dynamic pressure ratio for a shock of essentially zero strength. A modification to the relation was made so that it fits the HULL data, and the result is:

$$1/f = 1/(1 - 1.08\ B)^2 \qquad (6)$$

Equation 6 fits the unchoked HULL data for step shocks for the increase in dynamic pressure ratio with blockage ratio within $\pm$ 2 percent and provides a reasonable extrapolation to values of B larger than 0.3. Although Equation 3 provides a fit to the HULL data with even less error than Equation 6, the improvement is not significant; and the function does not provide a valid extrapolation to larger blockages. Thus in any further work using the HULL results for the increase in dynamic pressure ratio with blockage, Equation 6 should be used instead of Equation 3.

IX. COMPENSATION TECHNIQUES

In testing of vehicles such as a truck carrying a communications shelter in a large blast simulator, the initial shock loading dominates the blast damage response of the shelter and its contents, while the drag loading causes whole body movement and overturning. As shown in the previous study,[2] the increase in drag loading due to blockage will lower the minimum incident shock overpressure required for overturning (possibly below that desired for testing for shock diffraction effects). The decaying blast waves that would be tested in a large blast simulator have slow enough decay rates that a target which produces a significant blockage of the test section would cause a modification to the flow similar to that shown here for non-decaying shocks. The increased dynamic pressure near the target would result in a larger impulse delivered to the target over the duration of the positive overpressure phase of the wave and probably an increase in the duration of the positive phase itself. As far as the target is concerned, the blockage effects make the incident wave appear to be that from a higher-yield weapon at, most likely, some other burst point. Thus, the test is invalidated to some degree unless some means of systematically compensating for this apparent shift in yield and burst point is introduced.

In a target/blast wave encounter where the target is not grossly over-matched by the blast wave, it is the impulse in the drag phase that typically determines whether or not the target will be overturned. One means of compensating for the increase in impulse due to blockage effects is to reduce the duration (and hence the impulse) of the input blast wave so that the overturning limit occurs at the same minimum required incident shock overpressure as that of interest under free-field conditions. Therefore, the blast wave in the simulator would be for a smaller yield weapon at a closer range than the design (threat) weapon, with the yield and range reduction compensating exactly for the increase in impulse due to blockage.

The calculations of overturning performed earlier[2] were analzyed to derive the reduced duration and corresponding yield that, with the drag enhancement due to blockage, would produce overturning at the same overpressure as predicted for free-field conditions. The results are shown in Figure 21. As the blockage ratio is increased the duration and equivalent yield of the blast wave input to the test section decreases significantly. However, a proper use of this technique implies having a good prediction capability for overturning under known blast conditions and the ability to produce the desired reduced duration waveform, so its utility may be limited.

A wind tunnel experiment is described in Reference 9 which evaluates a technique for reducing blockage effects. The essence of the technique is to provide venting areas in the side walls of the test section to compensate for the reduction of the cross-sectional area of the tube because of the blockage by the target. This was done by "nesting" a sub-sized test section inside the larger wind tunnel test section. This sub-sized test section (hereinafter called "subsection" for brevity) was mounted on the floor of the wind tunnel. The subsection contained the target, which produced a blockage of the subsection of about 20 percent. Venting areas were provided in the sides and top walls of the subsection to compensate for the blockage caused by the target. The total area of the side vents equaled approximately 10 percent of the total cross-sectional area of the subsection. The floor was kept solid so that ground proximity effects would still occur.

With this arrangement, the low-velocity steady flow not only entered the subsection and interacted with the target but also flowed past the subsection between its side and top walls and the side and top walls of the wind tunnel test section. Therefore, the flow from region around the target and through the vent areas was into the wind tunnel free-stream conditions and not into ambient atmospheric conditions. Tests showed that the blockage correction constant, m, in Equation 4 was reduced from 1.9 to 0.75. This change corresponds to reducing the effects of 20 percent blockage of a test section with no open area to that for 8 percent blockage, a very significant reduction.

Although the flow in a blast simulator will not be steady-state as in the wind tunnel experiment, venting the simulator test section may produce a similar reduction of the increase in dynamic pressure in the constricted-flow region near the target for slowly-decaying blast waves. Venting might be accomplished by using many ports spaced uniformly around the side walls and roof of the test section and along its length.

The number and location of ports opened or closed would be adjusted according to the blockage produced by the target and its location in the test section. The pressure differential driving the flow through the ports to the atmosphere would be much larger in the simulator than that which prevailed in the wind tunnel experiment, and it is possible that the same percentage of open area would have a greater effect. The technique seems worth pursuing because it offers the possibility of reducing the blockage effect in the drag phase to a level that the effects of changes in orientation of the target would be small, and errors in interpretation of the magnitude of the changes produced by blockage would not be as important.

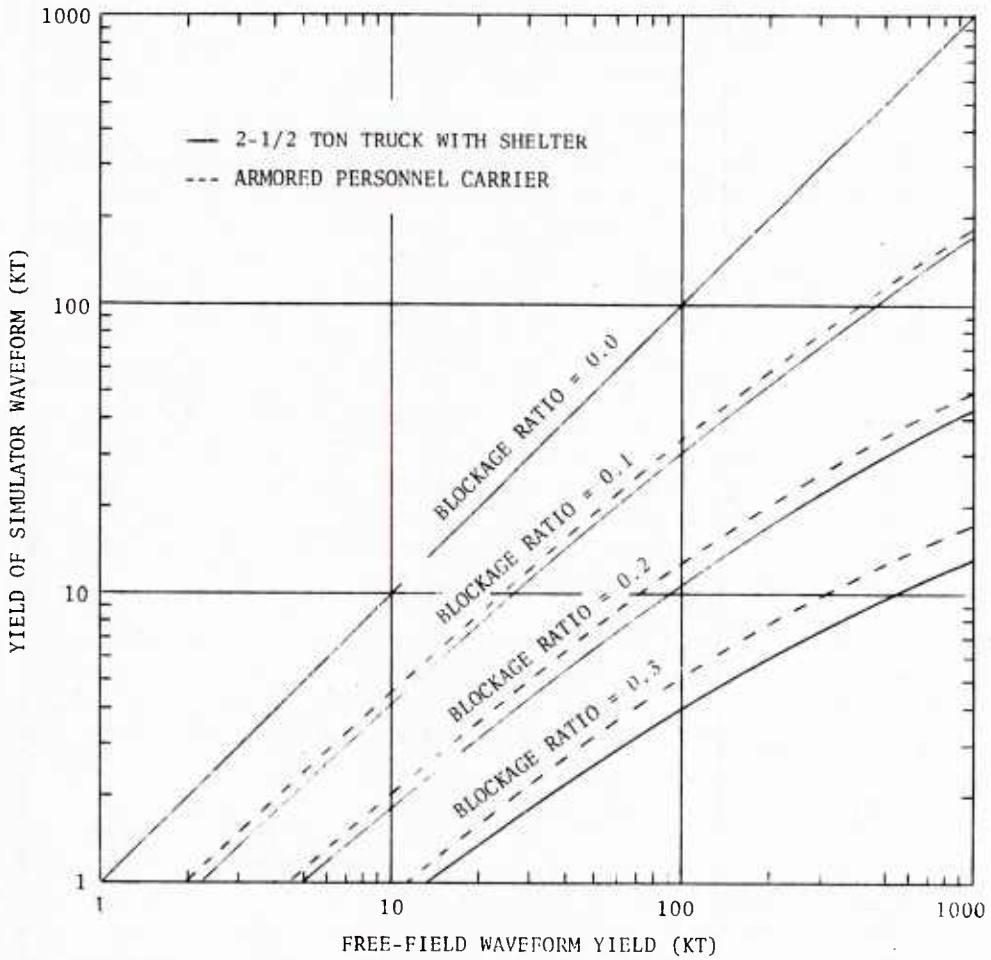

Figure 21. Yield of waveform input to simulator test section to cause overturning of vehicles versus free-field waveform yield to cause overturning at the same shock front overpressure for blockage ratios of 0.0, 0.1, 0.2, and 0.3. A blockage ratio of 0.0 corresponds to free-field conditions.

X. SUMMARY DISCUSSION

The HULL hydrocode has been utilized for studies of blockage effects for step shocks and for rapidly-decaying shocks. Comparisons were made between nozzle theory, shock tube experiments to measure drag force, and some low speed wind tunnel data. The comparisons indicate that the HULL results are reasonable.

Blockage effects in a large blast simulator may occur during both the diffraction and drag loading phases for the target. The importance of blockage effects will depend upon the purpose of the test, the target characteristics, the blockage ratio, and the input blast wave characteristics. During the initial shock/target interaction (diffraction phase), reflected waves are generated which expand from the target, strike the shock tube walls, and return to the target at relatively late time for the range of overpressures and blockages considered here. If the blockage is 30 percent or less, the net axial loading is not affected significantly during the diffraction phase. However, those reflected waves returning to the target produce added loading on the side faces because of their near-normal reflection from the target. This added side face loading may be enough to increase the deflection of light-construction side face walls of targets and so must be considered in the analysis of test results.

The dynamic pressure at the target is increased in proportion to the blockage for step shocks, slowly decaying waves, and rapidly decaying waves. The result for step and slowly decaying waves is an increase in drag loading which can change the target response significantly from that which would occur in free-field. If the input wave is rapidly decaying so that the diffraction loading predominates, this increase in drag loading is not important. If the rate of decay is sufficiently rapid, the increase in dynamic pressure is countered by the spatial static overpressure gradient; and the net axial loading becomes negative shortly after the diffraction loading phase ends. Thus the importance of the increase in dynamic pressure with blockage will depend upon the rate of decay of the input wave relative to the length of the target and the relative magnitudes of diffraction and drag loading. (Even if the decay of the input wave is sufficiently rapid that the drag loading on a target such as a vehicle is not important, the loading on smaller components attached to the exterior may be increased enough to be significant.)

Nozzle theory predictions of dynamic pressure enhancement versus blockage ratio agreed well with the HULL results for unchoked flow and show when choking conditions occur. The nozzle theory indicates that for 20 percent blockage, testing above 137.9 kPa (20 psi) will be at near-choking or choking conditions. At higher test pressures the blockage ratio that must be used to avoid choking decreases rapidly.

The flow configuration in the vicinity of the target changes with both blockage and incident shock strength. The spatial gradients of flow-field variables near the target are large. This is particularly true of dynamic pressure. This large variation must be considered in the placement of gages and in the interpretation of their measurements.

For tests involving slowly decaying shock waves in a shock tube, the dynamic pressure in the constricted-flow region increases as the blockage caused by the target increases. This produces a drag loading on the target which becomes increasingly larger in relative proportion to the diffraction phase loading experienced by the target. This causes the input blast wave to appear to the target as if it were from a larger-yield weapon at a greater distance away than that which was simulated to produce the pre-interaction blast wave. If the blockage is 20 percent or larger, significant changes in loading of the target can occur for the same input shock wave if the target orientation is changed. If the truck-shelter target were tested side-on at 20 percent blockage and then turned end-on for a second test, the blockage would be reduced to 10 percent. The effective drag impulse would be reduced by 30 percent, corresponding to a yield reduction by more than a factor of two. To properly design tests and utilize results from them under such conditions requires development of a body of knowledge concerning blockage effects versus target shape, placement in the test section, test section cross-sectional shape, target orientation, and other geometric parameters.

A wind tunnel experiment[9] demonstrated that by providing 10 percent open area in the test section walls, the effective blockage was reduced from 20 percent to 8 percent. The possibility of producing such large reductions in effective blockage in a blast simulator by using a test section with controlled venting seems worth pursuing.

REFERENCES

1. A.H. Shapiro, The Dynamics and Thermodynamics of Compressible Fluid Flow, Volumes I and II, Chpts 2, 4, and 25, The Ronald Press Company, New York, New York, 1953.

2. N.H. Ethridge, R.E. Lottero, J.D. Wortman, and B.P. Bertrand, "Flow Blockage and its Effect on Minimum Incident Overpressures for Overturning Vehicles in a Large Blast Simulator," Proceedings of the Seventh International Symposium on Military Applications of Blast Simulation, Vol. II, Medicine Hat, Alberta, Canada, 13-17 July 1981.

3. J.D. Wortman and R.E. Lottero, "Comparison of HULL Hydrocode Computations of Shock Tube Blockage Effects on Target Loading for Step Shocks and Rapidly-Decaying Shocks," ARBRL-MR-03232, U.S. Army Ballistic Research Laboratory, Aberdeen Proving Ground, MD, December 1982. (AD A123274)

4. C.E. Needham, M.L. Havens, and C.S. Knauth, "Nuclear Blast Standard (1 KT)," AFWL-TR-73-55(REV.), U.S. Air Force Weapons Laboratory, Kirtland Air Force Base, NM, April 1975. (AD#A014850)

5. N.H. Ethridge, "Blast Overturning Model for Ground Targets," Proceedings of the Fourth International Symposium on Military Applications of Blast Simulation, Southend-on-Sea, England, September 9-12, 1974.

6. J.R. Crosnier and J.B. Monzac, "Large Diameter High Performance Blast Simulator," Proceedings of the Fifth International Symposium on Military Applications of Blast Simulation, Stockholm, Sweden, May 23-26, 1977.

7. J.R. Crosnier, S. Gratias, J.B. Monzac, and H. Richard, "Concepts and Design for a Large Diameter High Performance Blast Simulator," Proceedings of the Fourth International Symposium on Military Applications of Blast Simulation, Southend-on-Sea, England, September 9-12, 1974.

8. G.A. Coulter and B.P. Bertrand, "BRL Shock Tube Facility for the Simulation of Air Blast Effects," US Army Ballistic Research Laboratory Memorandum Report No. 1685, August 1965. (AD#475669)

9. D.M. Sykes, "Blockage Corrections for Large Bluff Bodies in Wind Tunnels," Paper 18, Advances in Road Vehicle Aerodynamics, Edited by H.S. Stevens, BHRA FLuid Engineering, pp 311-322.

LIST OF SYMBOLS

f	-	Blockage correction factor, $1/Q_R$
m	-	Empirical constant, blockage correction relation
t	-	Time
v	-	Particle velocity
x	-	Displacement
A_i	-	nozzle inlet area
A_t	-	nozzle throat area
B	-	Blockage ratio, the ratio of target cross-sectional area to the blast simulator cross-sectional area
CD	-	Drag coefficient, adjusted for velocity
CD_o	-	Low velocity drag coefficient
KT	-	Kiloton TNT, blast equivalent
M	-	Cylinder mass
M_R	-	Mach number ratio, the local Mach number in the throat divided by the local Mach number behind the incident shock
Q_R	-	Dynamic pressure ratio, the dynamic pressure in the throat divided by the dynamic pressure behind the incident shock
ρ	-	Density
$1/2\ \rho v^2$	-	Dynamic pressure

DISTRIBUTION LIST

No. of Copies	Organization
12	Administrator Defense Technical Info Center ATTN: DTIC-DDA Cameron Station Alexandria, VA 22314
1	Director of Defense Research & Engineering ATTN: DD/TWP Washington, DC 20301
1	Asst. to the Secretary of Defense (Atomic Energy) ATTN: Document Control Washington, DC 20301
1	Director Defense Advanced Research Projects Agency ATTN: Tech Lib 1400 Wilson Boulevard Arlington, VA 22209
2	Director Federal Emergency Management Agency ATTN: John Nocita Technical Library Washington, DC 20472
1	Director Defense Intelligence Agency ATTN: DT-2/Wpns & Sys Div Washington, DC 20301
1	Director National Security Agency ATTN: E. F. Butala, R15 Ft. George G. Meade, MD 20755
1	Director Joint Strategic Target Planning Staff JCS Offut AFB Omaha, NE 68113
1	Director Defense Communications Agency ATTN: 930 Washington, DC 20305
9	Director Defense Nuclear Agency ATTN: DDST TIPL/Tech Lib SPSS/K. Goering G. Ullrich SPTD/T. Kennedy SPAS/P.R. Rohr STSP/COL Kovel NATD NATA Washington, DC 20305
2	Commander Field Command, DNA ATTN: FCPR FCTMOF Kirtland AFB, NM 87117
1	Commander Field Command, DNA Livermore Branch ATTN: FCPRL P.O. Box 808 Livermore, CA 94550
1	Director Inst for Defense Analyses ATTN: Library 1801 Beauregard St. Alexandria, VA 22311
1	Program Manager US Army BMD Program Office ATTN: John Shea 5001 Eisenhower Avenue Alexandria, VA 22333

DISTRIBUTION LIST

No. of Copies	Organization
2	Director US Army BMD Advanced Technology Center ATTN: CRDABH-X CRDABH-S Huntsville, AL 35807
1	Commander US Army BMD Command ATTN: BDMSC-TFN/N.J. Hurst P.O. Box 1500 Huntsville, AL 35807
1	Commander US Army Engineer Division ATTN: HNDED-FD P.O. Box 1500 Huntsville, AL 35807
2	Deputy Chief of Staff for Operations and Plans ATTN: Technical Library Director of Chemical & Nuc Operations Department of the Army Washington, DC 20310
2	Office, Chief of Engineers Department of the Army ATTN: DAEN-MCE-D DAEN-RDM 890 South Pickett Street Alexandria, VA 22304
3	Commander US Army Engineer Waterways Experiment Station ATTN: Technical Library William Flathau Leo Ingram P.O. Box 631 Vicksburg, MS 39180
1	Commander US Army Engineering Center ATTN: ATSEN-SY-L Fort Belvoir, VA 22060
1	US Army MERADCOM ATTN: DRDME-EM, D. Frink Fort Belvoir, VA 22060
1	Commander US Army Materiel Development and Readiness Command ATTN: DRCDMD-ST 5001 Eisenhower Avenue Alexandria, VA 22333
1	Commander Armament R&D Center US Army AMCCOM ATTN: DRSMC-TDC(D) Dover, NJ 07801
3	Commander Armament R&D Center US Army AMCCOM ATTN: DRSMC-LCN-F, W. Reiner DRSMC-TSS(D) Dover, NJ 07801
1	Commanmder US Army Armament, Munitions and Chemical Command ATTN: DRSMC-LEP-L (R) Rock Island, IL 61299
1	Director Benet Weapons Laboratory Armament R&D Center US Army AMCCOM ATTN: DRSMC-LCB-TL(D) Watervliet, NY 12189
1	Commander US Army Aviation Research and Development Command ATTN: DRDAV-E 4300 Goodfellow Boulevard St. Louis, MO 63120

DISTRIBUTION LIST

No. of Copies	Organization
1	Director US Army Air Mobility Research and Development Laboratory Ames Research Center Moffett Field, CA 94035
1	Commander US Army Communications Rsch and Development Command ATTN: DRSEL-ATDD Fort Monmouth, NJ 07703
3	Commander US Army Electronics R&D Command Technical Support Activity ATTN: DELSD-L DELEW-E, W. S. McAfee DELSD-EI, J. Roma Fort Monmouth, NJ 07703
8	Commander US Army Harry Diamond Labs ATTN: Mr. James Gaul Mr. L. Belliveau Mr. J. Meszaros Mr. J. Gwaltney Mr. F. W. Balicki Mr. Bill Vault Mr. R. J. Bostak Mr. R. K. Warner 2800 Powder Mill Road Adelphi, MD 20783
4	Commander US Army Harry Diamond Labs ATTN: DELHD-TA-L DRXDO-TI/002 DRXDO-NP DELHD-RBA/J. Rosado 2800 Powder Mill Road Adelphi, MD 20783

No. of Copies	Organization
1	Commander US Army Missile Command ATTN: DRSMI-YDL Redstone Arsenal, AL 35898
1	Commander US Army Missile Command ATTN: DRSMI-R Redstone Arsenal, AL 35898
3	Commander US Army Natick Research and Development Laboratories ATTN: DRXRE/Dr. D. Sieling DRXNE-UE/A. Johnson W. Crenshaw Natick, MA 01760
1	Commander US Army Tank Automotive Automotive Command ATTN: DRSTA-TSL Warren, MI 48090
1	Comander US Army Foreign Science and Technology Center ATTN: Rsch & Concepts Br 220 7th Street , NE Charlottesville, VA 22901
1	Commander US Army Logistics Management Ctr ATTN: ATCL-O Mr. Robert Cameron Fort Lee, VA 23801
3	Commander US Army Materials and Mechanics Research Center ATTN: Technical Library DRXMR-ER, Joe Prifti Eugene de Luca Watertown, MA 02172

DISTRIBUTION LIST

No. of Copies	Organization
1	Commander US Army Research Office P.O. Box 12211 Research Triangle Park NC 27709
4	Commander US Army Nuclear & Chemical Agency ATTN: ACTA-NAW MONA-WE Technical Library MAJ Uecke 7500 Backlick Rd, Bldg. 2073 Springfield, VA 22150
1	Commander US Army TRADOC ATTN: DCST&E Fort Monroe, VA 23651
2	Director US Army TRADOC Systems Analysis Activity ATTN: LTC John Hesse ATAA-SL White Sands Missile Range NM 8802
1	Commander US Combined Arms Combat Developments Activity ATTN: ATCA-CO, Mr. L. C. Pleger Fort Leavenworth, KS 66027
2	Commandant US Army Infantry School ATTN: ATSH-CO-CSO-OR Fort Benning, GA 31905
1	Commandant Interservice Nuclear Weapons School ATTN: Technical Library Kirtland AFB, NM 87117

No. of Copies	Organization
1	Chief of Naval Material ATTN: MAT 0323 Department of the Navy Arlington, VA 22217
2	Chief of Naval Operations ATTN: OP-03EG OP-985F Department of the Navy Washington, DC 20350
1	Office of Naval Research ATTN: N. Perrone Department of the Navy Arlington, VA 22217
1	Director Strategic Systems Projects Ofc ATTN: NSP-43, Tech Library Department of the Navy Washington, DC 20360
1	Commander Naval Electronic Systems Com ATTN: PME 117-21A Washington, DC 20360
1	Commander Naval Facilities Engineering Command Washington, DC 20360
1	Commander Naval Sea Systems Command ATTN: SEA-62R Department of the Navy Washington, DC 20362
3	Officer-in-Charge (Code L31) Civil Engineering Laboratory Naval Constr Btn Center ATTN: Stan Takahashi R. J. Odello Technical Library Port Hueneme, CA 93041

DISTRIBUTION LIST

No. of Copies	Organization
1	Commander David W. Taylor Naval Ship Research & Development Ctr ATTN: Lib Div, Code 522 Bethesda, MD 20084
1	Commander Naval Surface Weapons Center ATTN: DX-21, Library Br. Dahlgren, VA 22448
2	Commander Naval Surface Weapons Center ATTN: Code WA501/Navy Nuclear Programs Office Code WX21/Tech Library Silver Spring, MD 20910
1	Commander Naval Weapons Center ATTN: Code 533, Tech Lib China Lake, CA 93555
1	Commander Naval Weapons Evaluation Fac ATTN: Document Control Kirtland Air Force Base NM 87117
1	Commander Naval Research Laboratory ATTN: Code 2027, Tech Lib Washington, DC 20375
1	Superintendent Naval Postgraduate School ATTN: Code 2124, Technical Reports Library Monterey, CA 93940
1	AFSC/SDOA Andrews Air Force Base MD 20334
1	ADTC/DLODL, Tech Lib Eglin AFB, FL 32542
1	AFWL/SUL Kirtland AFB, NM 87117

No. of Copies	Organization
1	AFATL (DLYV) Eglin AFB, FL 32542
1	RADC (EMTLD/Docu Libray) Griffiss AFB, NY 13441
1	AFWL/NTES (R. Henny) Kirtland AFB, NM 87117
1	AFWL/NTE, CPT J. Clifford Kirtland AFB, NM 87117
2	Commander-in-Chief Strategic Air Command ATTN: NRI-STINFO Lib Offutt AFB, NE 68113
1	AFIT (Lib Bldg. 640, Area B) Wright-Patterson AFB Ohio 45433
1	FTD/NIIS Wright-Patterson AFB Ohio 45433
1	Director Lawrence Livermore Lab. ATTN: Tech Info Dept L-3 P.O. Box 808 Livermore, CA 94550
2	Director Los Alamos Scientific Lab ATTN: Doc Control for Rpts Lib P.O. Box 1663 Los Alamos, NM 87544
2	Director Sandia Laboratories ATTN: Doc Control for 3141 Sandia Report Collection L. J. Vortman Albuquerque, NM 87115

DISTRIBUTION LIST

No. of Copies	Organization
1	Director Sandia Laboratories Livermore Laboratory ATTN: Doc Control for Tech Lib P.O. Box 969 Livermore, CA 94550
1	Director National Aeronautics and Space Administration Scientific & Tech Info Fac P.O. Box 8757 Baltimore/Washington International Airport MD 21240
1	Aerospace Corporation ATTN: Tech Info Services P.O. Box 92957 Los Angeles, CA 90009
1	Agbabian Associates ATTN: M. Agbabian 250 North Nash Street El Segundo, CA 90245
1	The BDM Corporation ATTN: Richard Hensley P.O. Box 9274 Albuquerque International Albuquerque, NM 87119
1	The Boeing Company ATTN: Aerospace library P.O. Box 3707 Seattle, WA 98124
2	California Research and Technology ATTN: M. Rosenblatt F. Sauer 20943 Devonshire Street Chatsworth, CA 91311
1	Carpenter Research Corporation ATTN: H. Jerry Carpenter 6230 Scotmist Drive Rancho Palos Verdes, CA 90274
1	Goodyear Aerospace Corp ATTN: R. M. Brown, Bldg 1 Shelter Engineering Litchfield Park, AZ 85340
5	Kaman AviDyne ATTN: Dr. N.P. Hobbs (4 cys) Mr. S. Criscione 83 Second Avenue Northwest Industrial Park Burlington, MA 01803
3	Kaman Sciences Corporation ATTN: Library P. A. Ellis F. H. Shelton 1500 Garden of the Gods Road Colorado Springs, CO 80907
1	AFWL/SUL Kirtland AFB, NM 87117
1	Kaman Sciences Corporation ATTN: Don Sachs Suite 703 2001 Jefferson Davis Highway Arlington, VA 22202
1	Kaman-TEMPO ATTN: DASIAC P.O. Drawer QQ Santa Barbara, CA 93102
1	Kaman-TEMPO ATTN: E. Bryant, Suite UL-1 715 Shamrock Road Bel Air, MD 21014

DISTRIBUTION LIST

No. of Copies	Organization
1	Lockheed Missiles & Space Co. ATTN: J. J. Murphy, Dept. 81-11, Bldg. 154 P.O. Box 504 Sunnyvale, CA 94086
1	Martin Marietta Aerospace Orlando Division ATTN: G. Fotieo P.O. Box 5837 Orlando, FL 32805
2	McDonnell Douglas Astronautics Company ATTN: Robert W. Halprin Dr. P. Lewis 5301 Bolsa Avenue Huntington Beach, CA 92647
2	The Mitre Corporation ATTN: Library J. Calligeros, Mail Stop B-150 P.O. Box 208 Bedford, MA 01730
1	New Mexico Engineering Research Institute (CERF) ATTN: J. Leigh P.O. Box 25 UNM Albuquerque, NM 87131
1	Physics International 2700 Merced Street San Leandro, CA 94577
1	Radkowski Associates ATTN: Peter R. Radkowski P.O. Box 5474 Riverside, CA 92517
3	R&D Associates ATTN: Jerry Carpenter Technical Library Allan Kuhl P.O. Box 9695 Marina del Rey, CA 90291
1	RCA Government Communications Systems 13-5-2 Front & Cooper Streets Camden, NJ 08102
2	Science Applications, Inc. ATTN: Burton S. Chambers John Cockayne PO BOX 1303 1710 Goodridge Drive McLean, VA 22102
1	Science Applications, Inc. ATTN: Technical Library 1250 Prospect Plaza La Jolla, CA 92037
1	Systems, Science and Software ATTN: C. E. Needham PO Box 8243 Albuquerque, NM 87108
3	Systems, Science and Software ATTN: Technical Library R. Duff K. Pyatt PO Box 1620 La Jolla, CA 92037
1	TRW Electronics & Defense ATTN: Benjamin Sussholtz One Space Park Redondo Beach, CA 92078

DISTRIBUTION LIST

No. of Copies	Organization
2	Union Carbide Corporation Holifield National Laboratory ATTN: Doc Control for Tech Lib Civil Defense Research Proj PO Box X Oak Ridge, TN 37830
1	Weidlinger Assoc. Consulting Engineers 110 East 59th Street New York, NY 10022
1	Battelle Memorial Institute ATTN: Technical Library 505 King Avenue Columbus, OH 43201
1	California Inst of Tech ATTN: T. J. Ahrens 1201 E. California Blvd. Pasadena, CA 91109
2	Denver Research Institute University of Denver ATTN: Mr. J. Wisotski Technical Library PO Box 10127 Denver, CO 80210
1	IIT Research Institute ATTN: Milton R. Johnson 10 West 35th Street Chicago, IL 60616
1	TRW Ballistic Missile Division ATTN: H. Korman, Mail Station 526/614 P.O. Box 1310 San Bernadino, CA 92402
1	J. D. Haltiwanger Consulting Services B106a Civil Engineering Bldg. 208 N. Romine Street Urbana, IL 61801
1	Massachusetts Institute of Technology Aeroelastic and Structures Research Laboratory ATTN: Dr. E. A. Witmer Cambridge, MA 02139
2	Southwest Research Institute ATTN: Dr. W. E. Baker A. B. Wenzel 8500 Culebra Road San Antonio, TX 78228
1	SRI International ATTN: Dr. G. R. Abrahamson 333 Ravenswood Avenue Menlo Park, CA 94025
1	Stanford University ATTN: Dr. D. Bershader Durand Laboratory Stanford, CA 94305
1	Washington State University Physics Department ATTN: G. R. Fowles Pullman, VA 99163
	Aberdeen Proving Ground
	Dir, USAMSAA ATTN: DRXSY-D DRXSY-MP, H. Cohen Cdr, USATECOM ATTN: DRSTE-TO-F Cdr, CRDC, AMCCOM ATTN: DRSMC-CLB-PA DRSMC-CLN DRSMC-CLJ-L

USER EVALUATION OF REPORT

Please take a few minutes to answer the questions below; tear out this sheet, fold as indicated, staple or tape closed, and place in the mail. Your comments will provide us with information for improving future reports.

1. BRL Report Number _____

2. Does this report satisfy a need? (Comment on purpose, related project, or other area of interest for which report will be used.)

_____

_____

_____

3. How, specifically, is the report being used? (Information source, design data or procedure, management procedure, source of ideas, etc.) _____

_____

_____

4. Has the information in this report led to any quantitative savings as far as man-hours/contract dollars saved, operating costs avoided, efficiencies achieved, etc.? If so, please elaborate.

_____

_____

5. General Comments (Indicate what you think should be changed to make this report and future reports of this type more responsive to your needs, more usable, improve readability, etc.) _____

_____

_____

_____

6. If you would like to be contacted by the personnel who prepared this report to raise specific questions or discuss the topic, please fill in the following information.

Name: _____

Telephone Number: _____

Organization Address: _____

_____

_____

FOLD HERE

Director
US Army Ballistic Research Laboratory
ATTN: DRSMC-BLA-S (A)
Aberdeen Proving Ground, MD 21005

NO POSTAGE
NECESSARY
IF MAILED
IN THE
UNITED STATES

OFFICIAL BUSINESS
PENALTY FOR PRIVATE USE, $300

BUSINESS REPLY MAIL
FIRST CLASS PERMIT NO 12062 WASHINGTON, DC
POSTAGE WILL BE PAID BY DEPARTMENT OF THE ARMY

Director
US Army Ballistic Research Laboratory
ATTN: DRSMC-BLA-S (A)
Aberdeen Proving Ground, MD 21005

FOLD HERE